Electronic Supporting Information:

Tuning Extreme Anisotropic Thermal Expansion in 1D Coordination Polymers through Metal Selection and Solid Solutions

Lisa M. van Wyk, Leigh Loots and Leonard J. Barbour*

Department of Chemistry and Polymer Science, University of Stellenbosch, 7602 Matieland, South Africa.

* Correspondence to Professor Leonard J. Barbour (Email: ljb@sun.ac.za)

Contents

1. Crystallisation procedures

1.1. Crystallisation of ZnCP

{[Zn(bpdc)(bpy)]·2DMF}$_n$ (**ZnCP**) was prepared solvothermally. In a scintillation vial, equimolar amounts of the ligands 4,4'-biphenyldicarboxylic acid (bpdc, 0.10 mmol, 24.2 mg) and 2,2'-bipyridine (bpy, 0.10 mmol, 15.6 mg), along with Zn(NO$_3$)$_2$·6H$_2$O (0.15 mmol, 44.8 mg) were added to 3 ml DMF and sonicated until partially dissolved. The vial was placed in an 80 °C preheated oven for 3 days. Clear, rod-shaped crystals were produced (**Fig. S1**).
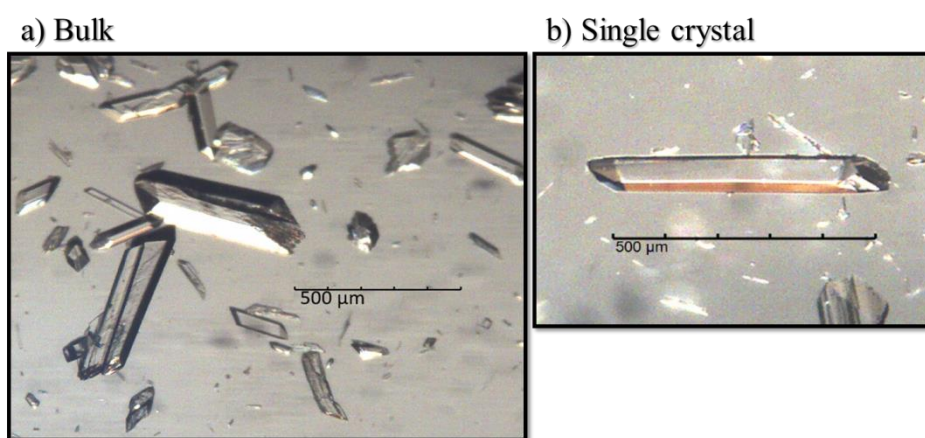
1.2. Crystallisation of CoCP

Figure S1: Photomicrographs of the bulk crystallisation (**a**) and a single crystal (**b**) of **ZnCP**.

Single crystals of {[Co(bpdc)(bpy)]·2DMF}$_n$ (**CoCP**) were prepared similarly to the procedure in **§1.1**. However, Co(NO$_3$)$_2$·6H$_2$O (0.15 mmol, 30.2 mg) was utilised in place of Zn(NO$_3$)$_2$·6H$_2$O. Clusters of dark pink rod-shaped crystals were produced (**Fig. S2**).

Figure S2: Photomicrographs of the bulk crystallisation (**a**) and a single crystal (**b**) of **CoCP**.

1.3. Crystallisation of CdCP

Single crystals of {[Cd(bpdc)(bpy)]·2DMF}$_n$ (**CdCP**) were prepared similarly to the procedure in **§1.1**. However, Cd(NO$_3$)$_2$·4H$_2$O (0.15 mmol, 46.3 mg) was utilised in place of Zn(NO$_3$)$_2$·6H$_2$O. The solvothermal temperature was also adjusted to 100 °C. Clear, rod-shaped crystals were produced (**Fig. S3**).
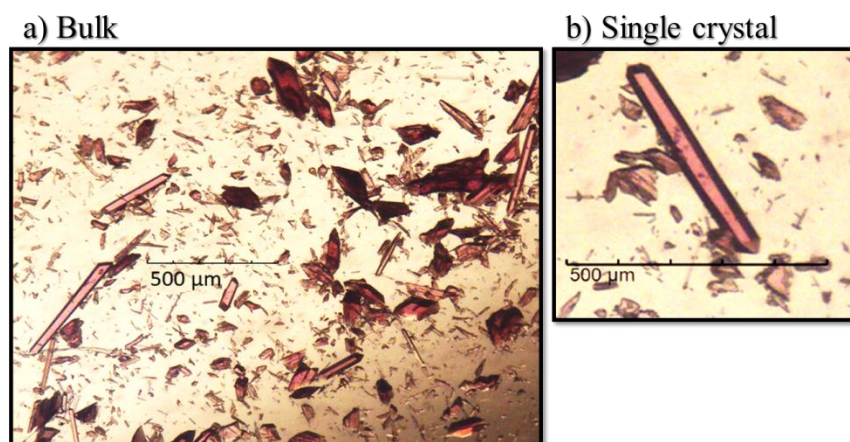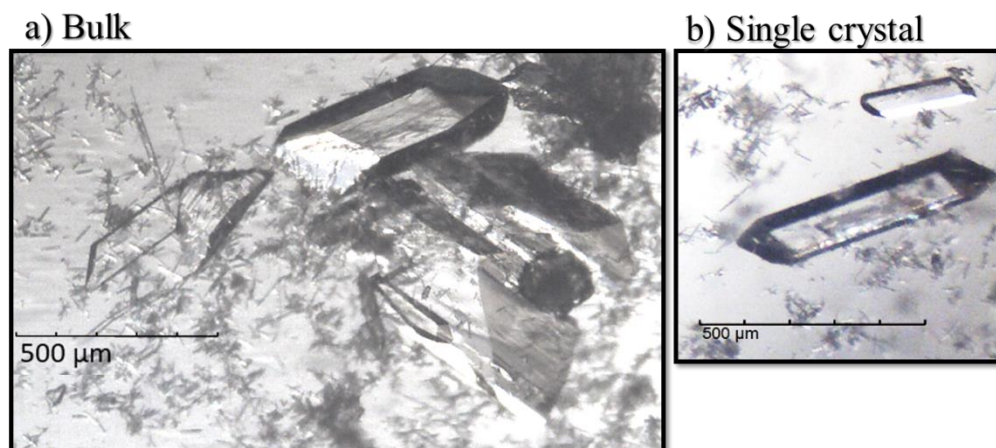

Figure S3: Photomicrographs of the bulk crystallisation (**a**) and single crystals (**b**) of **CdCP**.

1.4. Crystallisation of NiCP

Single crystals of {[Ni(bpdc)(bpy)]·2DMF}$_n$ (**NiCP**) were prepared similarly to the procedure in **§1.1**. However, Ni(NO$_3$)$_2$·6H$_2$O (0.15 mmol, 43.6 mg) was utilised in place of Zn(NO$_3$)$_2$·6H$_2$O. Intergrown teal rod-shaped crystals were produced (**Fig. S4**).

Figure S4: Photomicrographs of the bulk crystallisation (**a**) and single crystals (**b**) of **NiCP**.

1.5. Crystallisation of ZnCoCP

Single crystals of $\{[Zn_{0.92}Co_{0.08}(bpdc)(bpy)]\cdot2DMF\}_n$ (**ZnCoCP**) were prepared similarly to the procedure in **§1.1**. However, both $Zn(NO_3)_2\cdot6H_2O$ (0.08 mmol, 22.4 mg) and $Co(NO_3)_2\cdot6H_2O$ (0.08 mmol, 15.1 mg) were utilised. Clusters of light pink rod-shaped crystals were produced (**Fig. S5**).
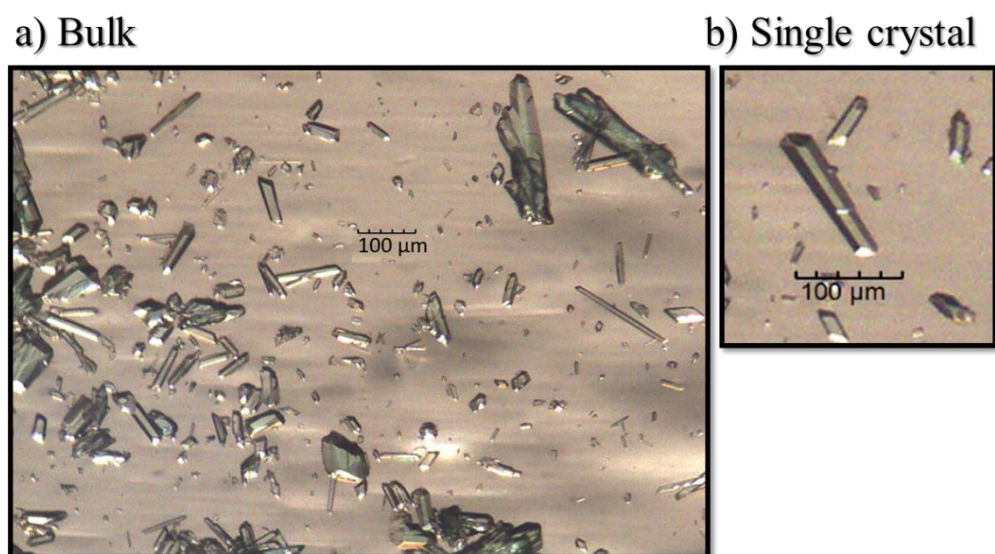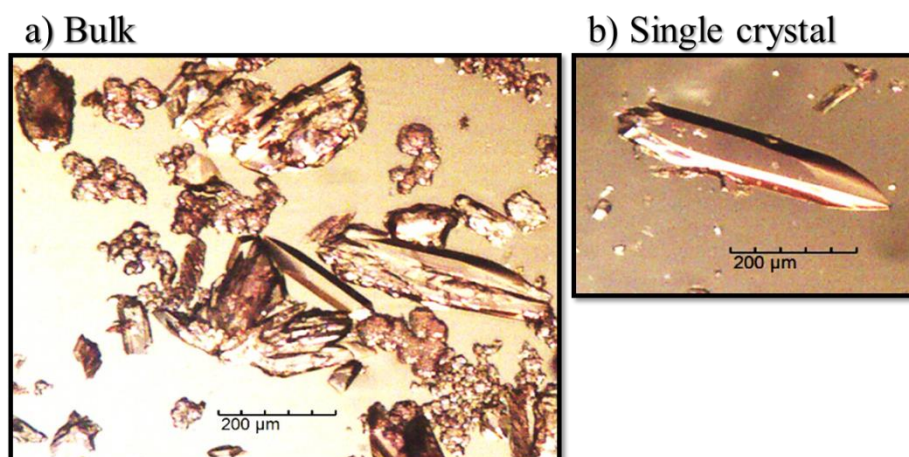

Figure S5: Photomicrographs of the bulk crystallisation **(a)** and a single crystal **(b)** of **ZnCoCP**.

1.6. Crystallisation of NiCdCP

Single crystals of $\{[Ni_{0.83}Cd_{0.17}(bpdc)(bpy)]\cdot2DMF\}_n$ (**NiCdCP**) were prepared similarly to the procedure in **§1.1**. However, both $Cd(NO_3)_2\cdot4H_2O$ (0.08 mmol, 23.2 mg) and $Ni(NO_3)_2\cdot6H_2O$ (0.08 mmol, 21.8 mg) were utilised. The solvothermal temperature was also adjusted to 100 °C. Green rod-shaped crystals were produced (**Fig. S6**).

Figure S6: Photomicrographs of the bulk crystallisation **(a)** and a single crystal **(b)** of **NiCdCP**.

1.7. Crystallisation of ZnCdCP

Single crystals of $\{[Zn_{0.92}Cd_{0.08}(bpdc)(bpy)]\cdot2DMF\}_n$ (**ZnCdCP**) were prepared similarly to the procedure in **§1.1**. However, both $Zn(NO_3)_2\cdot6H_2O$ (0.08 mmol, 22.4 mg) and $Cd(NO_3)_2\cdot4H_2O$ (0.08 mmol, 23.2 mg) were utilised. The solvothermal temperature was also adjusted to 100 °C. Clear rod-shaped crystals were produced (**Fig. S7**).
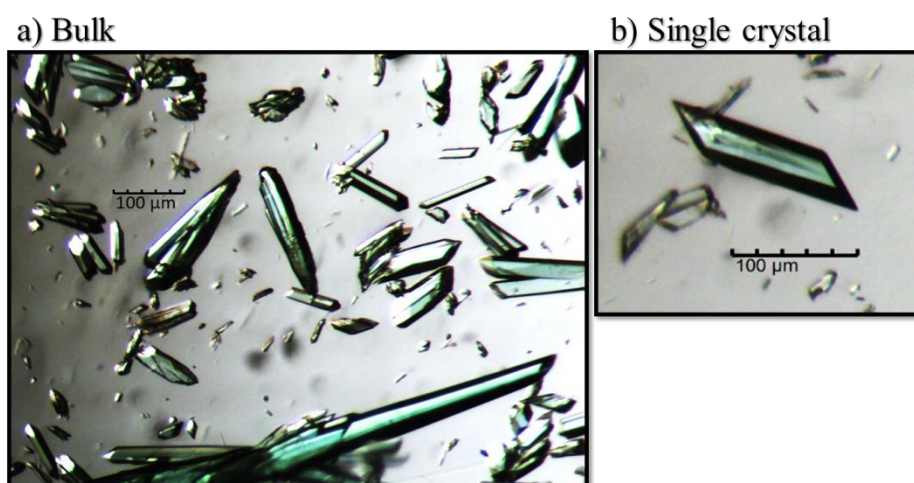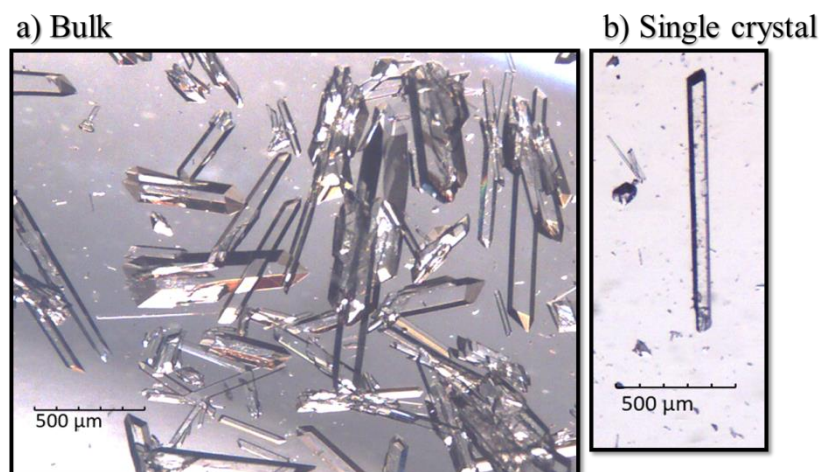

Figure S7: Photomicrographs of the bulk crystallisation **(a)** and a single crystal **(b)** of **ZnCdCP**.

2. Single-crystal X-ray diffraction (SCXRD)

Crystals of appropriate size and morphology, and the ability to extinguish plane-polarized light were attached to the tip of a MiTeGen mount[1] using Paratone®N oil. The crystal mount was then attached to a goniometer head, which was in turn mounted on a diffractometer. X-ray intensity data were recorded using either a Bruker APEX II DUO or a Bruker D8 Venture diffractometer. The DUO instrument is equipped with Incoatec IµS molybdenum (λ = 0.71073 Å) and copper (λ = 1.5418 Å) microfocus X-ray sources and a CCD area detector. The Venture instrument is equipped with an Incoatec IµS 3.0 molybdenum (λ = 0.71073 Å) microfocus X-ray source and a Photon II CPAD detector. Each diffractometer is equipped with an Oxford Cryosystems cryostat (700 Series Cryostream Plus for the DUO instrument and 800 Series Cryostream Plus for the Venture instrument), which is used to control the sample temperature. Both the frame exposure time and the number of frames collected for each experiment were varied, depending on the diffraction quality and characteristics of the mounted crystal.

Data reduction and absorption corrections were carried out using the SAINT[2] and SADABS[3] programs, respectively. The unit-cell dimensions were refined on all data and space groups were assigned based on systematic absences and intensity statistics. The structures were solved with a dual-space algorithm or direct methods using SHELXT[4] or SHELXS-2016/1,[5] respectively. Structure refinement was carried out with SHELXL-2018/3[5] using the X-Seed[6,7] graphical user interface. Non-hydrogen atoms were refined anisotropically. Hydrogen atoms were placed in calculated positions. Illustrations of all crystal structures were generated using the programs POV-Ray[8] and Mercury.[9–11]

Please note that the structural determinations of the separate phases for each material were carried out on different crystals.
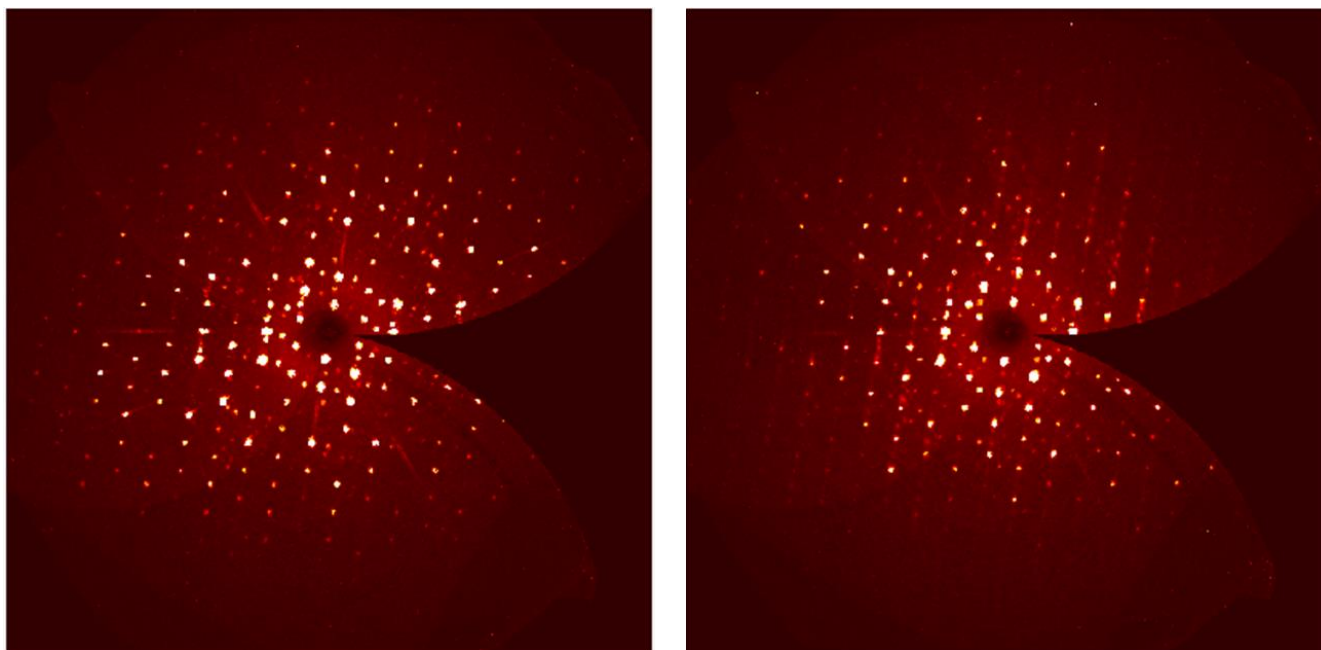
Figure S8: Precession images of a single crystal of **ZnCP** showing the *h0l* plane. The image on the left shows the crystal at 270 K while the image on the right shows the same crystal at 100 K (fast cooling so as not to shock the crystal). The crystal exhibits poorer diffraction at 100 K.

Table S1. Crystallographic parameters for the full structural determination of the materials studied.

	ZnCP^{HT}	ZnCP^{LT}	NiCP^{HT}	NiCP^{LT}	CoCP^{HT}	CoCP^{LT}	CdCP^{HT}	CdCP^{LT}
Empirical Formula	$C_{30}H_{30}N_4O_6Zn$	$C_{30}H_{30}N_4O_6Zn$	$C_{30}H_{30}N_4O_6Ni$	$C_{30}H_{30}N_4O_6Ni$	$C_{30}H_{30}N_4O_6Co$	$C_{30}H_{30}N_4O_6Co$	$C_{30}H_{30}N_4O_6Cd$	$C_{30}H_{30}N_4O_6Cd$
Formula weight (g mol^{-1})	607.94	607.94	601.28	601.28	601.50	601.50	654.97	654.97
Temperature (K)	270(2)	100(2)	270(2)	100(2)	270(2)	100(2)	270(2)	100(2)
Wavelength (Å)	0.71073	0.71073	0.71073	0.71073	0.71073	0.71073	0.71073	0.71073
Crystal system	Monoclinic	Monoclinic	Monoclinic	Monoclinic	Monoclinic	Monoclinic	Monoclinic	Monoclinic
Space group	$P2_1/n$	$P2_1/n$	$P2_1/n$	$P2_1/n$	$P2_1/n$	$P2_1/n$	$P2_1/n$	$P2_1/n$
a (Å)	7.700(4)	7.598(1)	7.587(1)	7.696(1)	7.672(5)	7.580(3)	7.751(1)	7.635(1)
b (Å)	25.487(13)	26.508(5)	26.025(1)	28.012(6)	25.683(18)	25.608(11)	23.773(1)	22.768(3)
c (Å)	17.427(8)	16.115(3)	16.934(6)	14.695(3)	17.291(13)	16.702(7)	19.044(1)	19.177(2)
α (°)	90	90	90	90	90	90	90	90
β (°)	99.18(1)	99.22(3)	99.26(1)	99.71(1)	98.63(2)	97.96(1)	96.40(1)	94.90(1)
γ (°)	90	90	90	90	90	90	90	90
V (Å^3)	3376.0(30)	3204.0(11)	3301.0(2)	3122.6(11)	3369.0(40)	3211.0(20)	3487.3(4)	3321.5(7)
Z	4	4	4	4	4	4	4	4
Calculated density / (g cm^{-3})‡	0.908	0.957	0.916	0.968	0.898	0.942	0.969	1.017
Absorption coefficient (mm^{-1})	0.748	0.788	0.609	0.644	0.530	0.556	0.646	0.679
F_{000}	944.0	944.0	936.0	936.0	932.0	932.0	1016.0	1016.0
θ range for data collection (°)	2.37–26.02	2.00–28.38	1.42–26.02	1.58–25.08	2.38–25.03	1.47–26.48	2.74–27.88	2.31–28.31
Miller index ranges	$-8 \leq h \leq 9$ $-31 \leq k \leq 31$ $-21 \leq l \leq 21$	$-10 \leq h \leq 10$ $-35 \leq k \leq 35$ $-21 \leq l \leq 21$	$-9 \leq h \leq 9$ $-32 \leq k \leq 31$ $-20 \leq l \leq 20$	$-9 \leq h \leq 9$ $-33 \leq k \leq 33$ $-17 \leq l \leq 17$	$-9 \leq h \leq 8$ $-30 \leq k \leq 30$ $-20 \leq l \leq 20$	$-9 \leq h \leq 9$ $-31 \leq k \leq 32$ $-20 \leq l \leq 19$	$-10 \leq h \leq 8$ $-31 \leq k \leq 31$ $-25 \leq l \leq 25$	$-10 \leq h \leq 10$ $-30 \leq k \leq 30$ $-25 \leq l \leq 25$
Reflections collected	34409	85516	57798	27343	21224	21695	73044	48126
Independent reflections	6651	8016	6499	5760	5944	6485	8298	8254
Completeness to θ$_{max}$ (%)	99.9	99.8	99.9	98.9	99.9	97.6	99.9	99.7
Max. and min. transmission	0.260, 0.216	0.746, 0.700	0.260, 0.233	0.745, 0.576	0.260, 0.208	0.745, 0.647	0.263, 0.224	0.746, 0.665
Refinement Method	Full-matrix least-squares on F^2	Full-matrix least-squares on F^2	Full-matrix least-squares on F^2	Full-matrix least-squares on F^2	Full-matrix least-squares on F^2	Full-matrix least-squares on F^2	Full-matrix least-squares on F^2	Full-matrix least-squares on F^2
Data / restraints / parameters	6651 / 1512 / 552	8016 / 1837 / 552	5499 / 1533 / 552	5491 / 1563 / 552	5944 / 1524 / 552	6485 / 1503 / 552	8298/ 1539 / 552	8254 / 1509 / 552
Goodness-of-fit on F^2	1.010	1.020	1.040	1.129	1.013	1.033	1.016	1.117
Final R indices [$I > 2\sigma(I)$]	$R1$ = 0.0514 $wR2$ = 0.1455	$R1$ = 0.0405 $wR2$ = 0.1040	$R1$ = 0.0358 $wR2$ = 0.1004	$R1$ = 0.0850 $wR2$ = 0.1952	$R1$ = 0.0693 $wR2$ = 0.1754	$R1$ = 0.0530 $wR2$ = 0.1333	$R1$ = 0.0410 $wR2$ = 0.0991	$R1$ = 0.0469 $wR2$ = 0.1046
Largest diff. peak and hole (e A^{-3})	0.418, -0.427	0.467, -0.513	0.211, -0.199	0.653, -1.077	0.405, -0.554	0.531, -0.580	0.316, -0.587	0.932, -1.281

‡Densities calculated with structures that have had the guest electron density removed by the Platon/SQUEEZE[12] routine

Table S2. Crystallographic parameters for the full structural determination of the CPs studied (cont'd).

	ZnCoCP[HT]	ZnCoCP[LT]	NiCdCP[HT]	NiCdCP[LT]	ZnCdCP[HT]	ZnCdCP[LT]
Empirical Formula	$C_{30}H_{30}N_4O_6Zn_{0.92}$ $Co_{0.08}$	$C_{30}H_{30}N_4O_6Zn_{0.92}$ $Co_{0.08}$	$C_{30}H_{30}N_4O_6Ni_{0.83}$ $Cd_{0.17}$	$C_{30}H_{30}N_4O_6Ni_{0.83}$ $Cd_{0.17}$	$C_{30}H_{30}N_4O_6Zn_{0.92}$ $Cd_{0.08}$	$C_{30}H_{30}N_4O_6Zn_{0.92}$ $Cd_{0.08}$
Formula weight (g mol^{-1})	607.42	607.42	610.4	610.4	611.7	611.7
Temperature (K)	270(2)	100(2)	270(2)	100(2)	270(2)	100(2)
Wavelength (Å)	0.71073	0.71073	0.71073	0.71073	0.71073	0.71073
Crystal system	Monoclinic	Monoclinic	Monoclinic	Monoclinic	Monoclinic	Monoclinic
Space group	$P2_1/n$	$P2_1/n$	$P2_1/n$	$P2_1/n$	$P2_1/n$	$P2_1/n$
a (Å)	7.716(2)	7.600(1)	7.632(1)	7.501(1)	7.696(1)	7.604(1)
b (Å)	25.819(6)	26.519(1)	26.288(6)	25.985(1)	25.461(1)	26.523(1)
c (Å)	17.144(4)	16.029(1)	16.739(4)	16.598(1)	17.429(1)	16.123(1)
α (°)	90	90	90	90	90	90
β (°)	99.26(1)	99.21(1)	98.90(1)	98.15(1)	99.02(1)	99.05(1)
γ (°)	90	90	90	90	90	90
V (Å^3)	3370.8(14)	3189.2(1)	3317.9(12)	3202.5(2)	3373.1(4)	3211.1(3)
Z	4	4	4	4	4	4
Calculated density / (g cm^{-3})‡	0.909	0.961	0.929	0.963	0.917	0.963
Absorption coefficient (mm^{-1})	0.732	0.774	0.618	0.641	0.742	0.780
F_{000}	943	943	949.6	949.6	950	949.8
θ range for data collection (°)	1.44–25.35	1.50–26.02	2.58–25.03	1.47–26.02	2.50–26.73	1.49–26.41
Miller index ranges	$-9 \leq h \leq 9$ $-31 \leq k \leq 31$ $-20 \leq l \leq 20$	$-9 \leq h \leq 9$ $-32 \leq k \leq 32$ $-19 \leq l \leq 19$	$-9 \leq h \leq 8$ $-31 \leq k \leq 31$ $-19 \leq l \leq 19$	$-9 \leq h \leq 9$ $-32 \leq k \leq 32$ $-20 \leq l \leq 20$	$-9 \leq h \leq 9$ $-32 \leq k \leq 32$ $-22 \leq l \leq 22$	$-9 \leq h \leq 9$ $-33 \leq k \leq 33$ $-20 \leq l \leq 20$
Reflections collected	69300	67084	48308	55707	66170	58598
Independent reflections	6175	6283	5839	6303	7157	6582
Completeness to θ$_{max}$ (%)	100	99.9	99.8	99.9	99.8	99.7
Max. and min. transmission	0.260, 0.202	0.745, 0.698	0.259, 0.191	0.746, 0.659	0.263, 0.218	0.745, 0.707
Refinement Method	Full-matrix least-squares on F^2	Full-matrix least-squares on F^2	Full-matrix least-squares on F^2	Full-matrix least-squares on F^2	Full-matrix least-squares on F^2	Full-matrix least-squares on F^2
Data / restraints / parameters	6175 / 1590 / 561	6283 / 1620 / 561	5839 / 1595 / 561	6303 / 1610 / 561	7157 / 1583 / 555	6582 / 1579 / 561
Goodness-of-fit on F^2	1.050	1.055	1.038	1.120	1.032	1.090
Final R indices [$I > 2\sigma(I)$]	$R1 = 0.0627$ $wR2 = 0.1936$	$R1 = 0.0415$ $wR2 = 0.1238$	$R1 = 0.0694$ $wR2 = 0.1862$	$R1 = 0.0628$ $wR2 = 0.1500$	$R1 = 0.0461$ $wR2 = 0.1314$	$R1 = 0.0397$ $wR2 = 0.1180$
Largest diff. peak and hole (e A^{-3})	0.398, -0.511	0.513, -0.257	0.323, -0.650	0.874, -1.053	0.507, -0.384	0.429, -0.318

‡Densities calculated with structures that have had the guest electron density removed by the Platon/SQUEEZE[12] routine

2.1. Packing diagrams of the low temperature phases
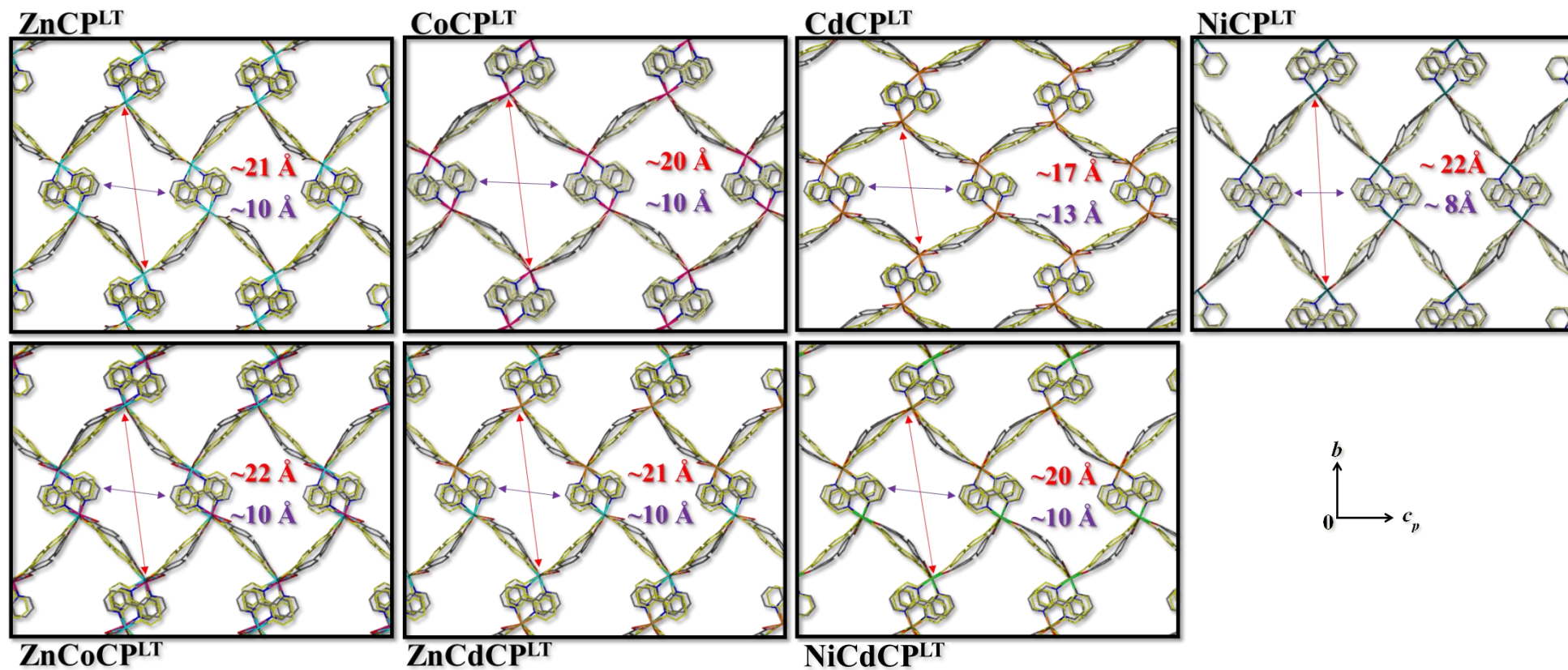
Figure S9: Packing of the low temperature phase (determined at 100 K) of each material studied viewed down the *a* axis. In each material both ligands are disordered over two positions. The minor component of disorder for each ligand is shown in yellow for clarity. The approximate channel aperture dimensions are indicated for each species. Both metal atoms are shown in the representations of the solid solutions, but may be superimposed. Guest molecules and hydrogen atoms have been omitted for clarity.

2.2. Probe accessible volume (PAV) maps

The PAV[13] for each species was investigated in Mercury[9–11] using a probe radius of 1.5 Å and a grid spacing of 0.2 Å.

Figure S10: PAV of the high temperature phase (270 K) of the materials studied viewed down the *a* axis. The PAV for the major components of ligand disorder are shown in the top row, while the minor components are shown in the bottom row. The percentage PAV of the unit-cell volume is also given in each case. Guest molecules have been omitted.

Figure S11: PAV of the high temperature (270 K) phase of the solid-solutions studied viewed down the *a* axis. The PAV for the major components of ligand disorder are shown in the top row, while the minor components are shown in the bottom row. The percentage PAV of the unit-cell volume is also given in each case. Both metal centres are shown, but may be superimposed. Guest molecules have been omitted.
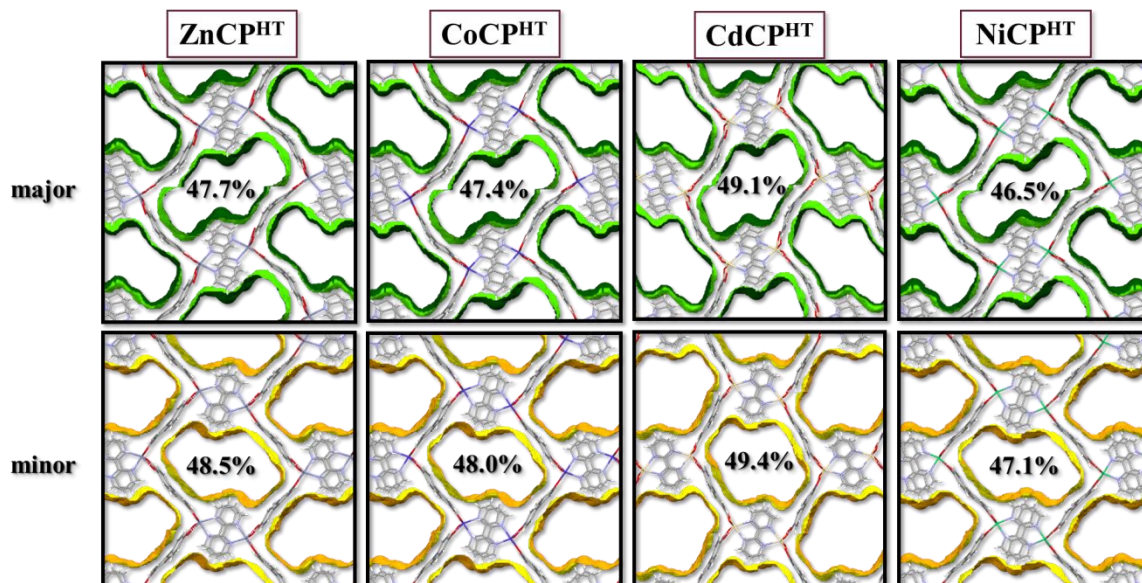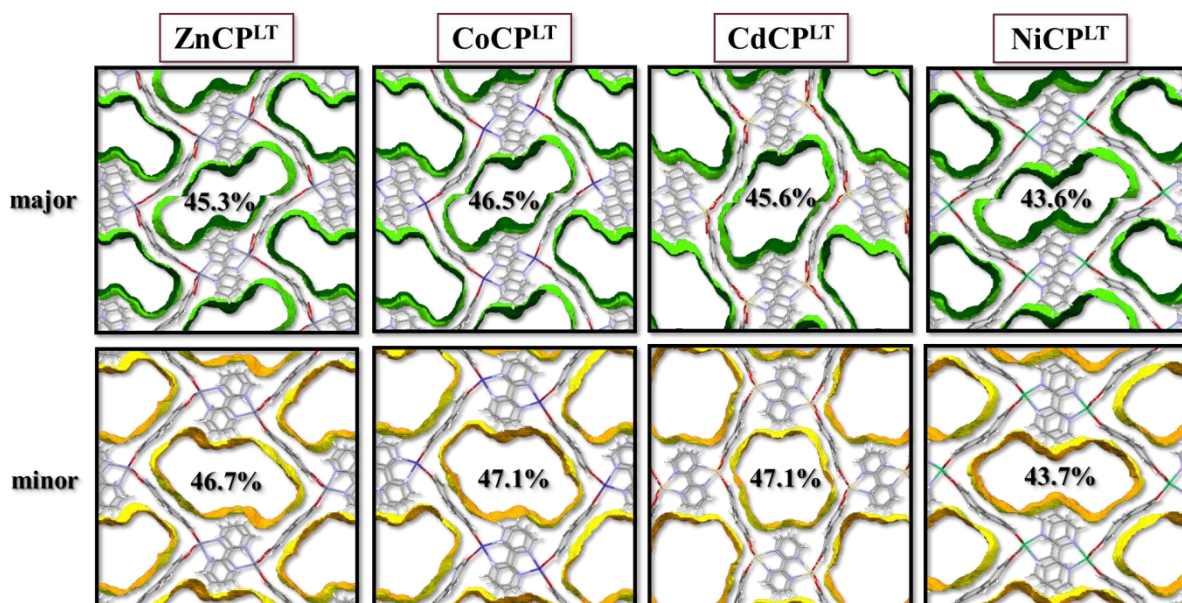
Figure S12: PAV of the low temperature phase (100 K) of the materials studied viewed down the *a* axis. The PAV for the major components of ligand disorder are shown in the top row, while the minor components are shown in the bottom row. The percentage PAV of the unit-cell volume is also given in each case. Guest molecules have been omitted.
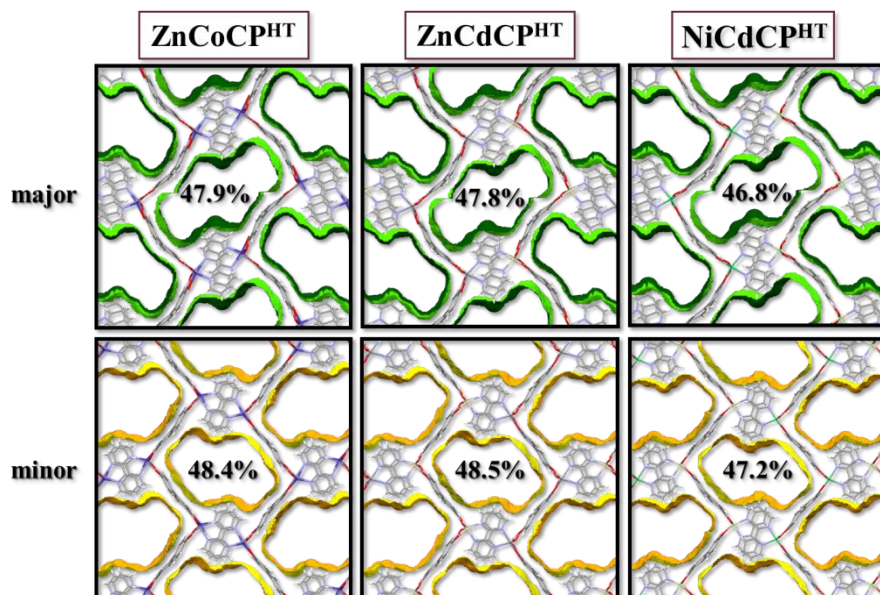

Figure S13: PAV of the low temperature phase (100 K) of the solid solutions studied viewed down the *a* axis. The PAV for the major components of ligand disorder are shown in the top row, while the minor components are shown in the bottom row. The percentage PAV of the unit-cell volume is also given in each case. Both metal centres are shown, but may be superimposed. Guest molecules have been omitted.
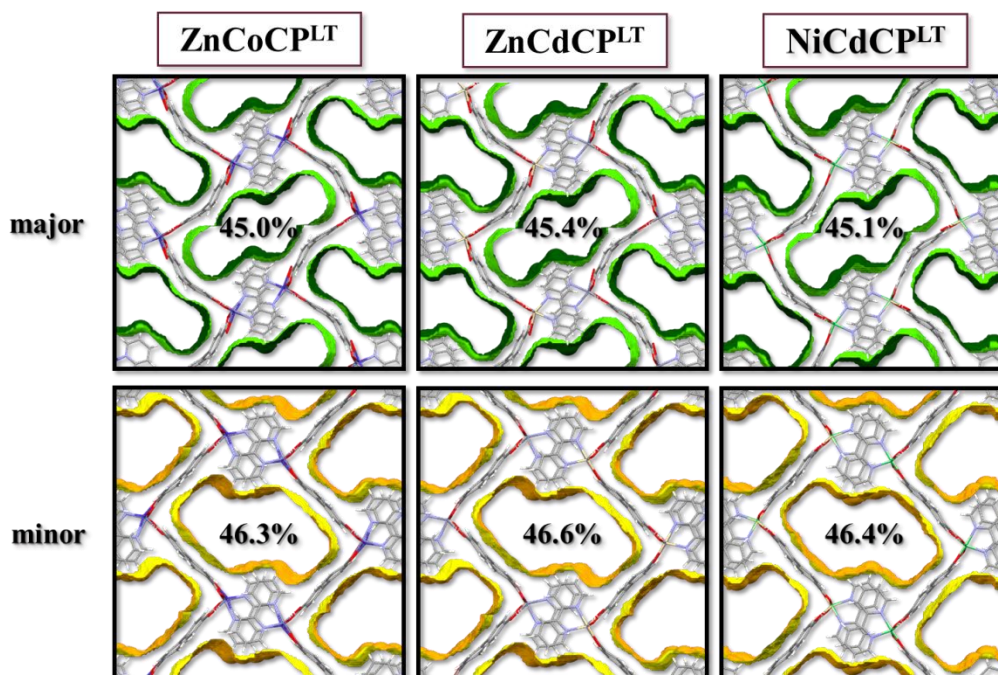
2.3. Variable-temperature unit-cell determinations

Variable-temperature unit-cell data were determined at 10 K intervals over a temperature range of 270–100 K. 270 K was chosen as the upper temperature limit owing to the facile desolvation of the compounds studied. These data were processed in the unit-cell tab of APEX3[14] as well as reduced with the SAINT[2] program (three iterations). Care was taken to remove anomalous scattering from the reciprocal lattice. In most cases the reduced data are presented. However, in the case of **CoCP** the loss of single crystal quality below 250 K led to the unreduced data presenting a more accurate depiction.

In cases where materials desolvate under the required experimental temperature an environmental solvent cell was employed. The solvent cell consists of a 1 mm diameter glass Lindemann Capillary attached to a steel nut with epoxy, which is then screwed into a placeholder body (allowing the solvent cell to be mounted to the goniometer). The capillary was filled with the same solvent that is the guest in the material of interest (*i.e.* DMF). A crystal was then positioned in the capillary on cotton wool (to keep it stationary). The capillary was capped by the placeholder body and attached to the goniometer. Subsequently, the data collection procedure was followed as above.

An environmental solvent cell was used to expand the upper temperature range in data collections for **CoCP**, **NiCP** and **NiCdCP** as their phase change temperature are high relative to the other CPs. Therefore, more data was required to accurately quantify the thermal expansion coefficients. Unit-cell determinations were carried out as above using the solvent cell in the temperature range 280–310 K. The solvent cell was heated to 310 K and cooled to provide cooling data for comparison to the low temperature experiments. However, we do note that this may lead to preconditioning of the crystals, resulting in differences in the unit-cell data as extrapolated from the differences from the 270–100 K.
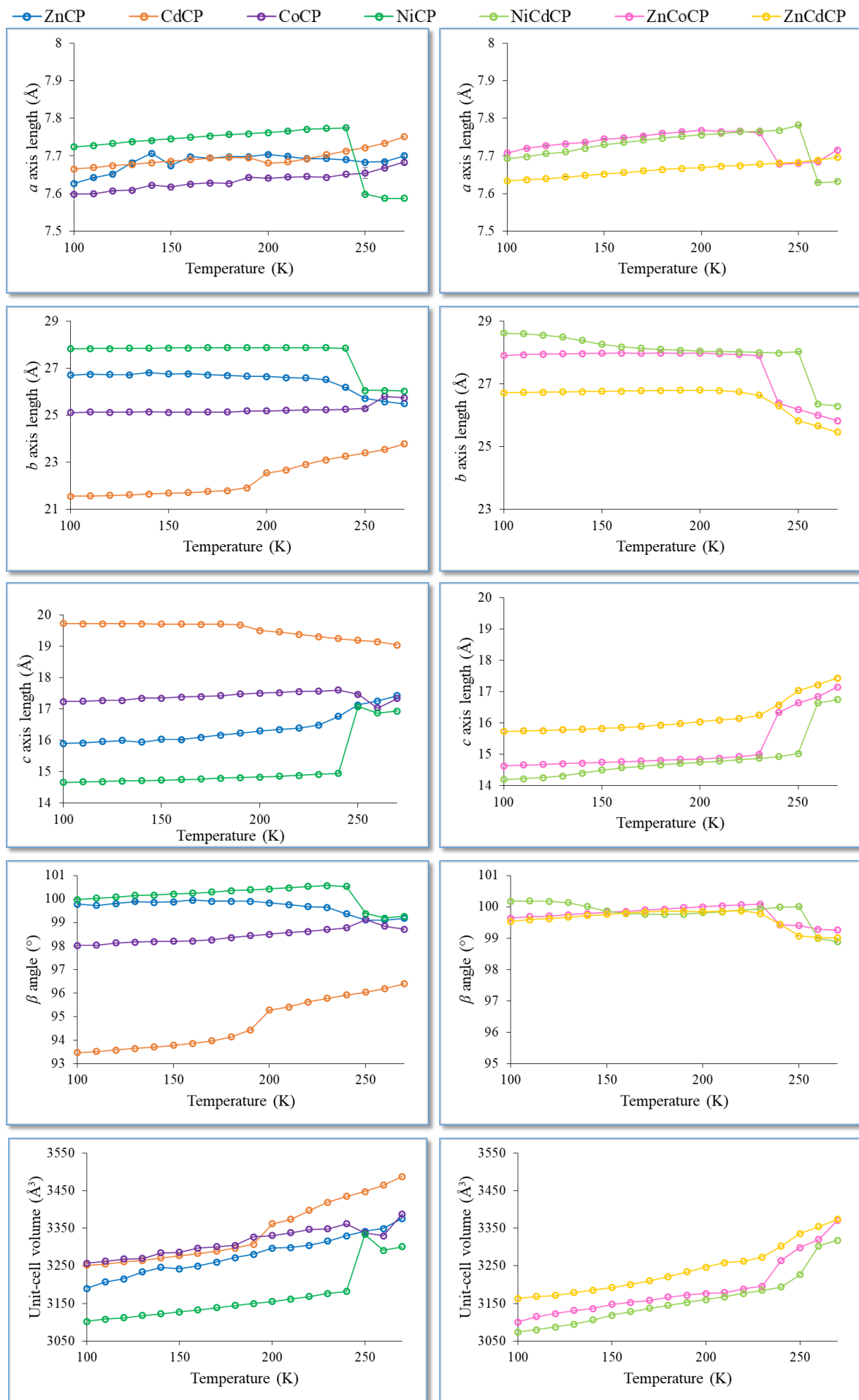
Figure S14: Variation of the unit-cell parameters over temperature of the materials in this study. Error bars are shown, but may be too small to discern.
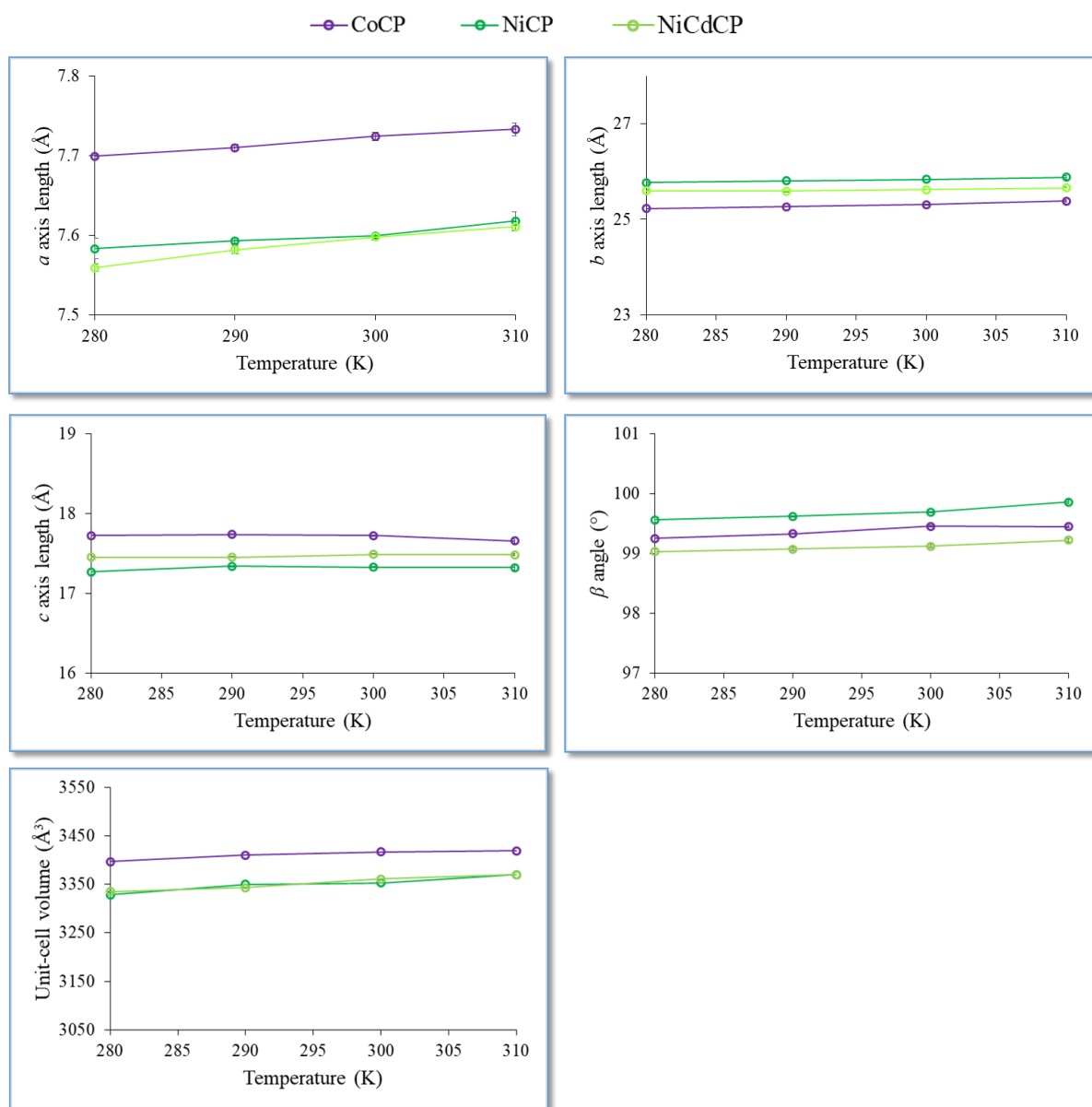
Figure S15: Variation of the unit-cell parameters over temperature for the environmental solvent cell experiments. Error bars are shown, but may be too small to discern.

Table S3. Variable-temperature unit-cell parameters as determined for **ZnCP**.

Temperature (K)	*a* axis (Å)	*b* axis (Å)	*c* axis (Å)	*β* angle (°)	Volume (Å³)
270	7.700(4)	25.487(13)	17.427(8)	99.18(1)	3376.3
260	7.685(2)	25.578(7)	17.254(5)	99.11(1)	3349.0
250	7.683(1)	25.720(5)	17.128(4)	99.11(1)	3341.9
240	**7.690(1)**	**26.181(8)**	**16.763(5)**	**99.37(1)**	**3330.0**
230	**7.693(2)**	**26.511(7)**	**16.490(4)**	**99.64(1)**	**3315.6**
220	7.693(2)	26.581(7)	16.393(4)	99.68(1)	3304.5
210	7.699(3)	26.592(10)	16.348(6)	99.76(1)	3298.7
200	7.704(3)	26.646(12)	16.301(7)	99.83(1)	3297.2
190	7.698(3)	26.652(13)	16.233(8)	99.90(1)	3280.9
180	7.698(4)	26.691(15)	16.166(9)	99.91(2)	3271.8
170	7.694(4)	26.718(17)	16.096(10)	99.91(2)	3259.6
160	7.698(5)	26.763(19)	16.021(11)	99.95(2)	3249.5
150	7.674(3)	26.752(10)	16.031(7)	99.88(3)	3242.0
140	7.707(6)	26.810(21)	15.944(12)	99.86(2)	3245.6
130	7.682(6)	26.710(30)	15.994(16)	99.89(3)	3234.0
120	7.652(3)	26.724(13)	15.958(8)	99.81(2)	3215.0
110	7.642(2)	26.743(12)	15.920(5)	99.73(1)	3207.0
100	7.627(3)	26.703(14)	15.896(9)	99.78(2)	3190.0
100‡	7.598(1)	26.508(5)	16.115(3)	99.22(3)	3204.0

*Values in bold indicate the phase transition region

‡Parameters determined from flash cooling (different crystal)

Table S4. Variable-temperature unit-cell parameters as determined for **NiCP**.

Temperature (K)	*a* axis (Å)	*b* axis (Å)	*c* axis (Å)	*β* angle (°)	Volume (Å³)
270	7.587(1)	26.025(1)	16.938(1)	99.26(1)	3301.0
260	7.587(1)	26.047(1)	16.872(1)	99.19(1)	3291.3
250	**7.598(2)**	**26.049(9)**	**17.073(6)**	**99.38(4)**	**3333.8**
240	**7.775(1)**	**27.849(4)**	**14.947(3)**	**100.54(1)**	**3182.0**
230	7.773(1)	27.865(4)	14.919(2)	100.57(1)	3176.6
220	7.771(1)	27.868(3)	14.884(2)	100.54(1)	3168.8
210	7.766(1)	27.866(3)	14.856(2)	100.48(1)	3161.6
200	7.762(1)	27.867(2)	14.831(1)	100.43(1)	3155.3
190	7.759(1)	27.868(1)	14.809(1)	100.39(1)	3149.5
180	7.757(1)	27.868(2)	14.790(1)	100.36(1)	3144.8
170	7.753(1)	27.865(2)	14.768(1)	100.30(1)	3138.9
160	7.749(1)	27.859(2)	14.748(1)	100.25(1)	3133.0
150	7.746(1)	27.853(2)	14.731(1)	100.22(1)	3127.8
140	7.741(1)	27.846(2)	14.715(1)	100.17(1)	3122.2
130	7.738(1)	27.842(2)	14.703(1)	100.16(1)	3118.0
120	7.733(1)	27.831(2)	14.688(1)	100.08(1)	3112.1
110	7.728(1)	27.830(2)	14.675(1)	100.04(1)	3107.9
100	7.724(1)	27.827(2)	14.656(1)	99.98(1)	3102.6
100[‡]	7.696(1)	28.012(5)	14.695(3)	99.71(3)	3122.6

*Values in bold indicate the phase transition region

[‡]Parameters determined from flash cooling (different crystal)

Table S5. Variable-temperature unit-cell parameters as determined for **CoCP**.

Temperature (K)	*a* axis (Å)	*b* axis (Å)	*c* axis (Å)	β angle (°)	Volume (Å^3)
270	7.672(5)	25.683(18)	17.291(13)	98.63(2)	3368.8
260	**7.668(2)**	**25.795(7)**	**17.036(5)**	**98.85(1)**	**3329.6**
250	**7.654(14)**	**25.291(50)**	**17.468(35)**	**98.13(5)**	**3338.3**
240	7.651(1)	25.253(4)	17.605(3)	98.78(1)	3361.7
230	7.643(1)	25.223(3)	17.570(2)	98.70(1)	3348.4
220	7.645(1)	25.222(3)	17.557(2)	98.62(1)	3347.1
210	7.644(1)	25.198(4)	17.527(3)	98.57(1)	3338.3
200	7.641(1)	25.179(4)	17.503(3)	98.50(1)	3330.6
190	7.643(1)	25.179(5)	17.476(3)	98.44(1)	3326.9
180	7.627(1)	25.137(5)	17.423(3)	98.36(1)	3304.8
170	7.628(1)	25.131(5)	17.398(4)	98.26(1)	3300.7
160	7.625(1)	25.131(5)	17.385(3)	98.22(1)	3297.0
150	7.618(1)	25.125(5)	17.348(3)	98.20(1)	3286.2
140	7.622(2)	25.148(6)	17.348(4)	98.19(1)	3284.7
130	7.609(1)	25.133(5)	17.275(3)	98.17(1)	3269.9
120	7.607(1)	25.121(6)	17.274(4)	98.13(1)	3267.9
110	7.599(1)	25.137(5)	17.250(3)	98.04(1)	3262.4
100	7.598(2)	25.105(6)	17.242(4)	98.02(1)	3256.7
100[‡]	7.580(3)	25.608(11)	16.702(7)	97.96(1)	3211.0

*Values in bold indicate the phase transition region

[‡]Parameters determined from flash cooling (different crystal)

Table S6. Variable-temperature unit-cell parameters as determined for **CdCP**.

Temperature (K)	*a* axis (Å)	*b* axis (Å)	*c* axis (Å)	*β* angle (°)	Volume (Å³)
270	7.751(1)	23.773(2)	19.044(1)	96.40(1)	3487.3
260	7.734(1)	23.535(1)	19.144(1)	96.19(1)	3464.4
250	7.722(1)	23.391(1)	19.191(1)	96.04(1)	3447.1
240	7.713(1)	23.258(1)	19.248(1)	95.92(1)	3434.4
230	7.703(1)	23.100(1)	19.311(1)	95.78(1)	3418.8
220	7.692(1)	22.902(1)	19.380(1)	95.62(1)	3397.5
210	7.684(1)	22.666(1)	19.459(1)	95.41(1)	3373.9
200	**7.681(1)**	**22.540(2)**	**19.501(2)**	**95.28(1)**	**3361.8**
190	**7.695(1)**	**21.903(2)**	**19.683(2)**	**94.43(1)**	**3307.6**
180	7.696(1)	21.794(2)	19.706(1)	94.13(1)	3296.9
170	7.694(1)	21.749(2)	19.704(1)	93.97(1)	3289.0
160	7.690(1)	21.711(2)	19.707(1)	93.86(1)	3282.7
150	7.686(1)	21.676(2)	19.711(1)	93.78(1)	3276.9
140	7.682(1)	21.643(1)	19.715(1)	93.70(1)	3270.8
130	7.677(2)	21.614(1)	19.715(1)	93.64(1)	3264.7
120	7.674(1)	21.590(1)	19.719(1)	93.58(1)	3260.6
110	7.669(1)	21.563(1)	19.719(1)	93.52(1)	3254.8
100	7.665(1)	21.547(1)	19.726(1)	98.47(1)	3251.9
100‡	7.635(1)	22.768(3)	19.177(2)	94.90(1)	3321.5

*Values in bold indicate the phase transition region

‡Parameters determined from flash cooling (different crystal)

Table S7. Variable-temperature unit-cell parameters as determined for **ZnCoCP**.

Temperature (K)	*a* axis (Å)	*b* axis (Å)	*c* axis (Å)	β angle (°)	Volume (Å^3)
270	7.716(2)	25.819(6)	17.144(4)	99.26(1)	3370.8
260	7.685(1)	26.001(1)	16.836(1)	99.29(2)	3319.9
250	7.680(1)	26.179(1)	16.632(1)	99.40(1)	3298.9
240	**7.678(4)**	**26.386(13)**	**16.335(9)**	**99.43(2)**	**3264.6**
230	**7.761(2)**	**27.902(8)**	**14.992(5)**	**100.09(1)**	**3196.2**
220	7.766(2)	27.937(5)	14.923(3)	100.06(1)	3188.2
210	7.765(1)	27.955(5)	14.874(3)	100.04(1)	3179.2
200	7.768(1)	27.981(5)	14.843(3)	100.00(1)	3177.0
190	7.764(2)	27.977(6)	14.828(3)	99.97(1)	3172.0
180	7.760(2)	27.984(6)	14.804(4)	99.93(1)	3166.7
170	7.753(2)	27.977(7)	14.780(4)	99.90(1)	3158.2
160	7.748(2)	27.979(7)	14.760(4)	99.86(1)	3152.5
150	7.745(2)	27.977(7)	14.744(4)	99.83(1)	3147.7
140	7.736(2)	27.961(7)	14.713(4)	99.79(1)	3136.1
130	7.732(2)	27.959(7)	14.695(4)	99.75(1)	3131.0
120	7.727(2)	27.945(7)	14.675(4)	99.71(1)	3123.3
110	7.720(2)	27.933(7)	14.654(4)	99.69(1)	3115.0
100	7.708(2)	27.904(7)	14.623(4)	99.64(1)	3101.0
100[‡]	7.600(1)	26.519(1)	16.029(1)	99.21(1)	3189.2

*Values in bold indicate the phase transition region

[‡]Parameters determined from flash cooling (different crystal)

Table S8. Variable-temperature unit-cell parameters as determined for **NiCdCP**.

Temperature (K)	*a* axis (Å)	*b* axis (Å)	*c* axis (Å)	β angle (°)	Volume (Å³)
270	7.632(2)	26.288(5)	16.739(4)	98.89(1)	3317.9
260	**7.629(1)**	**26.358(2)**	**16.632(1)**	**98.99(1)**	**3303.3**
250	**7.782(1)**	**28.029(3)**	**15.019(2)**	**100.01(1)**	**3266.3**
240	**7.768(1)**	**27.986(1)**	**14.918(1)**	**99.99(1)**	**3193.9**
230	7.766(1)	28.002(1)	14.868(1)	99.94(1)	3184.9
220	7.764(1)	28.014(1)	14.825(1)	99.89(1)	3176.4
210	7.760(1)	28.024(1)	14.783(1)	99.84(1)	3167.4
200	7.756(1)	28.043(1)	14.744(1)	99.81(1)	3160.2
190	7.752(1)	28.068(1)	14.704(1)	99.77(1)	3152.9
180	7.747(1)	28.096(2)	14.661(1)	99.76(1)	3144.9
170	7.742(1)	28.131(1)	14.615(1)	99.77(1)	3137.0
160	7.736(1)	28.178(1)	14.563(1)	99.79(1)	3128.3
150	7.730(1)	28.259(1)	14.492(1)	99.87(1)	3118.7
140	7.720(2)	28.382(1)	14.394(1)	100.01(1)	3105.8
130	7.711(2)	28.491(1)	14.310(1)	100.13(1)	3094.9
120	7.706(1)	28.555(1)	14.256(1)	100.18(1)	3087.5
110	7.698(1)	28.595(1)	14.214(1)	100.19(1)	3079.6
100	7.693(1)	28.617(1)	14.187(1)	100.18(1)	3074.2
100[‡]	7.501(1)	25.985(1)	16.598(1)	98.15(1)	3202.5

*Values in bold indicate the phase transition region

[‡]Parameters determined from flash cooling (different crystal)

Table S9. Variable-temperature unit-cell parameters as determined for **ZnCdCP**.

Temperature (K)	*a* axis (Å)	*b* axis (Å)	*c* axis (Å)	β angle (°)	Volume (Å³)
270	7.696(1)	25.460(2)	17.433(1)	99.01(1)	3373.9
260	7.689(1)	25.656(1)	17.216(1)	99.02(1)	3354.5
250	**7.683(1)**	**25.821(2)**	**17.027(1)**	**99.07(1)**	**3335.6**
240	**7.681(1)**	**26.299(2)**	**16.576(1)**	**99.45(1)**	**3302.7**
230	**7.678(1)**	**26.631(2)**	**16.245(1)**	**99.79(1)**	**3273.3**
220	7.674(1)	26.744(1)	16.134(1)	99.88(1)	3262.4
210	7.673(1)	26.788(1)	16.090(1)	99.86(1)	3258.2
200	7.669(1)	26.797(2)	16.035(1)	99.85(1)	3246.9
190	7.667(1)	26.798(2)	15.977(1)	99.86(1)	3234.0
180	7.664(1)	26.786(2)	15.926(1)	99.86(1)	3220.9
170	7.660(1)	26.776(2)	15.885(1)	99.74(1)	3210.3
160	7.656(1)	26.768(2)	15.849(1)	99.80(1)	3200.5
150	7.652(1)	26.759(2)	15.819(1)	99.76(1)	3192.0
140	7.648(1)	26.753(2)	15.795(1)	99.72(1)	3185.6
130	7.644(1)	26.744(2)	15.774(1)	99.67(1)	3178.9
120	7.639(1)	26.729(2)	15.753(2)	99.63(1)	3171.5
110	7.637(1)	26.726(2)	15.743(1)	99.59(1)	3168.2
100	7.633(1)	26.717(11)	15.728(1)	99.54(1)	3163.0
100‡	7.604(1)	26.523(1)	16.123(1)	98.05(1)	3211.1

*Values in bold indicate the phase transition region

‡Parameters determined from flash cooling (different crystal)

Table S10. Variable-temperature unit-cell parameters as determined for **NiCP** (HT range, solvent cell).

Temperature (K)	*a* axis (Å)	*b* axis (Å)	*c* axis (Å)	β angle (°)	Volume (Å³)
310	7.618(11)	25.880(40)	17.320(30)	99.86(3)	3370
300	7.599(3)	25.833(10)	17.327(8)	99.69(1)	3353
290	7.593(3)	25.803(11)	17.341(8)	99.62(1)	3350
280	7.583(13)	25.770(40)	17.270(30)	99.56(4)	3328

Table S11. Variable-temperature unit-cell parameters as determined for **CoCP** (HT range, solvent cell).

Temperature (K)	a axis (Å)	b axis (Å)	c axis (Å)	β angle (°)	Volume (Å^3)
310	7.733(8)	25.380(30)	17.655(20)	99.44(2)	3419
300	7.724(5)	25.309(14)	17.722(10)	99.46(1)	3417
290	7.710(4)	25.266(13)	17.737(10)	99.33(1)	3410
280	7.699(2)	25.223(7)	17.723(5)	99.25(1)	3397

Table S12. Variable-temperature unit-cell parameters as determined for **NiCdCP** (HT range, solvent cell).

Temperature (K)	a axis (Å)	b axis (Å)	c axis (Å)	β angle (°)	Volume (Å^3)
310	7.611(6)	25.660(18)	17.483(14)	99.22(3)	3370
300	7.598(4)	25.621(12)	17.489(10)	99.12(3)	3361
290	7.582(5)	25.588(15)	17.452(11)	99.07(3)	3343
280	7.559(5)	25.600(11)	17.452(10)	99.03(4)	3335

2.4. Variable-temperature single-crystal structure determinations

Many attempts were made to determine successive structures of a single crystal over the phase change event. However, this process results in significant stress on the crystal and in all cases the data were deemed to be of insufficient quality for satisfactory structure solution and refinement. Nonetheless, in the case of **ZnCP**, **CdCP** and **NiCP** the data were adequate to model the metal atoms and measure the M···M···M distance in the 1D chain. The solid solutions were excluded from this analysis since the partial occupancy of either metal node would complicate this determination. This distance was then plotted in an attempt to illustrate the changes effected by the phase change in each material.

Table S13. Change in the M⋯M⋯M angle in **ZnCP**, **NiCP** and **CdCP** over the phase change.

Temperature (K)	M⋯M⋯M ZnCP (°)	M⋯M⋯M NiCP (°)	M⋯M⋯M CdCP (°)
270	125.34(3)	123.144(7)	135.999(7)
260	124.63(3)	122.956(14)	136.861(10)
250	**123.89(3)**	**123.310(30)**	137.385(10)
240	**121.66(3)**	**116.380(30)**	137.860(13)
230	**120.12(3)**	116.270(20)	138.379(13)
220	119.80(3)	116.200(20)	139.025(13)
210	119.69(4)	116.170(20)	139.818(13)
200	119.53(5)	116.146(19)	**140.242(16)**
190	119.31(5)	116.106(19)	**145.286(13)**
180	119.03(5)	116.085(19)	145.837(10)
170	118.76(6)	116.053(19)	146.077(10)
160	118.46(6)	116.023(19)	146.244(10)
150	118.78(9)	116.000(19)	146.378(10)
140	118.21(8)	115.970(19)	146.487(10)
130	118.12(7)	115.924(19)	146.573(10)
120	118.08(7)	115.907(19)	146.650(10)
110	118.10(7)	115.876(19)	146.720(10)
100	118.56(11)	115.840(19)	146.774(10)

*Values in bold indicate the phase transition region
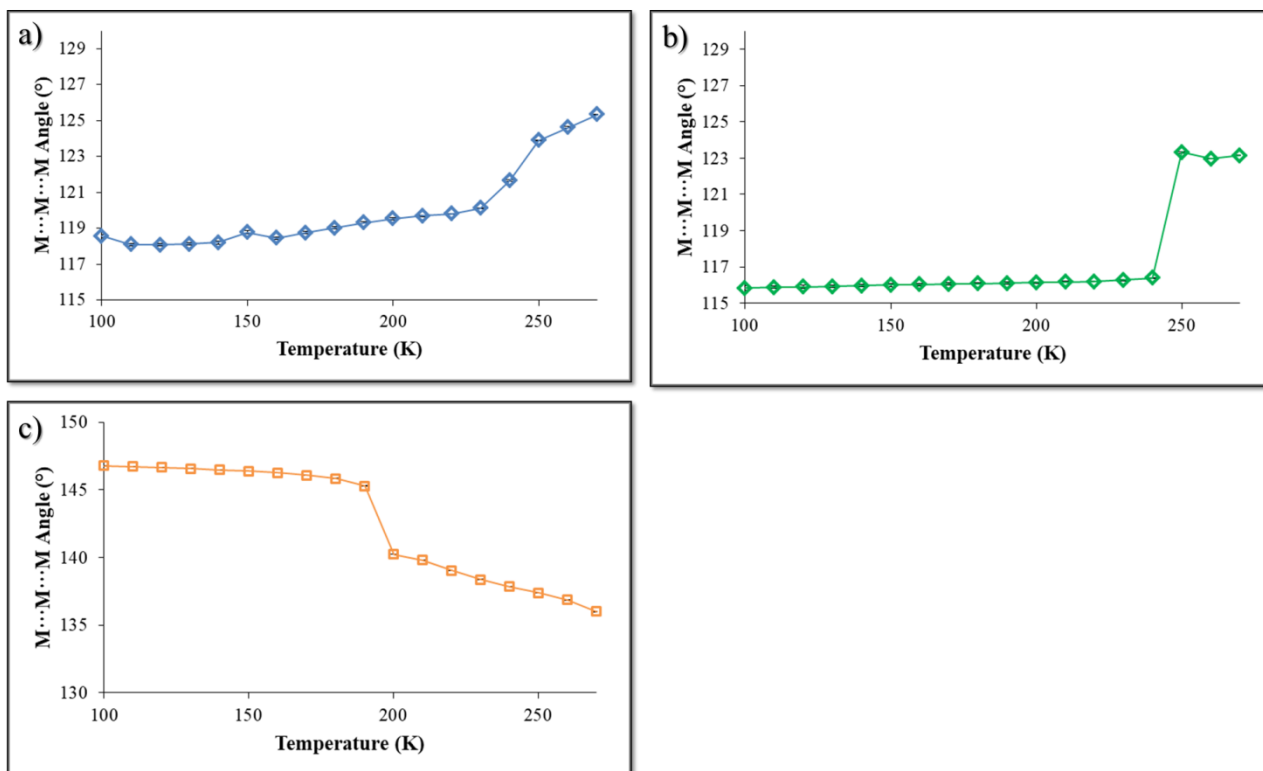
Figure S16: Variation in the M⋯M⋯M angle of the 1D chain as a function of temperature for **(a) ZnCP**, **(b) NiCP** and **(c) CdCP**. Error bars are shown, but may be too small to discern.

2.5. Temperature cycling of ZnCP to investigate flash cooling effect

To investigate possible attenuation of the phase change by changes in cooling rate, a SCXRD experiment was carried where the crystal was first cooled rapidly from 270 to 100 K (at a rate of 360 K h^{-1}) and its unit-cell parameters subsequently determined. Following this the crystal was heated to 270 K and then slowly cooled to 100 K (at a rate of 50 K h^{-1}) and the unit-cell parameters were determined again. Although this is not as dramatic as that seen in the variable temperature data it is important to note that the cooling rate is much lower in that case. However, the expected trend is observed, where the extent of the phase change is reduced with the higher cooling rate.

Table S14. Unit-cell parameters obtained from temperature cycling of **ZnCP**.

Temperature (K)	a axis (Å)	b axis (Å)	c axis (Å)	β angle (°)	Volume (Å^3)
270 (initial)	7.711(8)	25.516(30)	17.603(31)	99.28(6)	3418.3
100 (cooled at 360 K h^{-1})	7.605(1)	26.524(1)	16.027(1)	99.24(1)	3191.2
270 (heated at 360 K h^{-1})	7.703(1)	25.446(2)	17.489(2)	99.24(1)	3383.8
100 (cooled at 50 K h^{-1})	7.623(1)	26.644(2)	15.910(1)	99.47(1)	3187.2

3. Differential Scanning Calorimetry (DSC)

DSC was performed on either a TA Q20 instrument (analysis of **ZnCP**, **NiCP** and **CoCP**) or a TA Q100 instrument equipped with a Liquid Nitrogen Cooling System (analysis of **CdCP**). Samples of **ZnCP**, **NiCP**, **CoCP** and **CdCP** ranging in weight between 7 and 10 mg were placed in aluminium pans. The ramp rate was set at either 5 or 2 K min^{-1} to ascertain if a change in the rate of cooling would attenuate the energy of the phase transition. Each experiment was carried out in triplicate with a fresh sample used for each repetition. An N$_2$ gas flow rate of 50 ml min^{-1} was used. The resultant data were analysed using the TA Instruments Universal Analysis program.
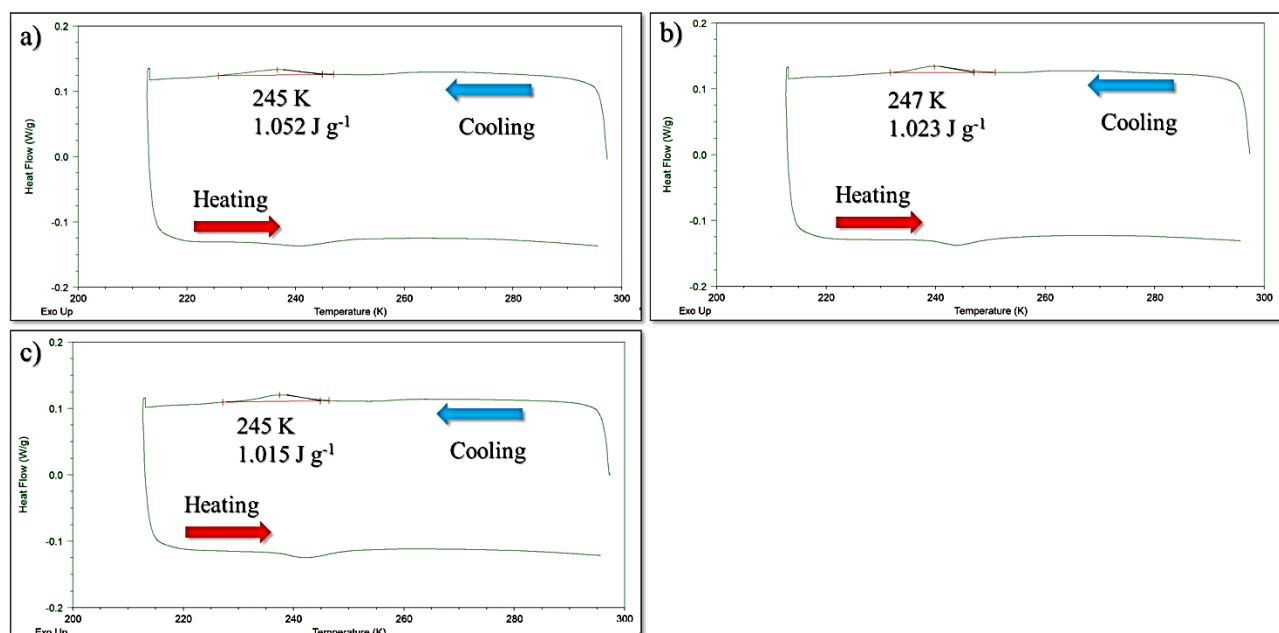
Figure S17: DSC thermograms for **ZnCP** cooled at 5 K min^{-1}. The onset temperature of the phase change and the peak integral are shown in each figure.
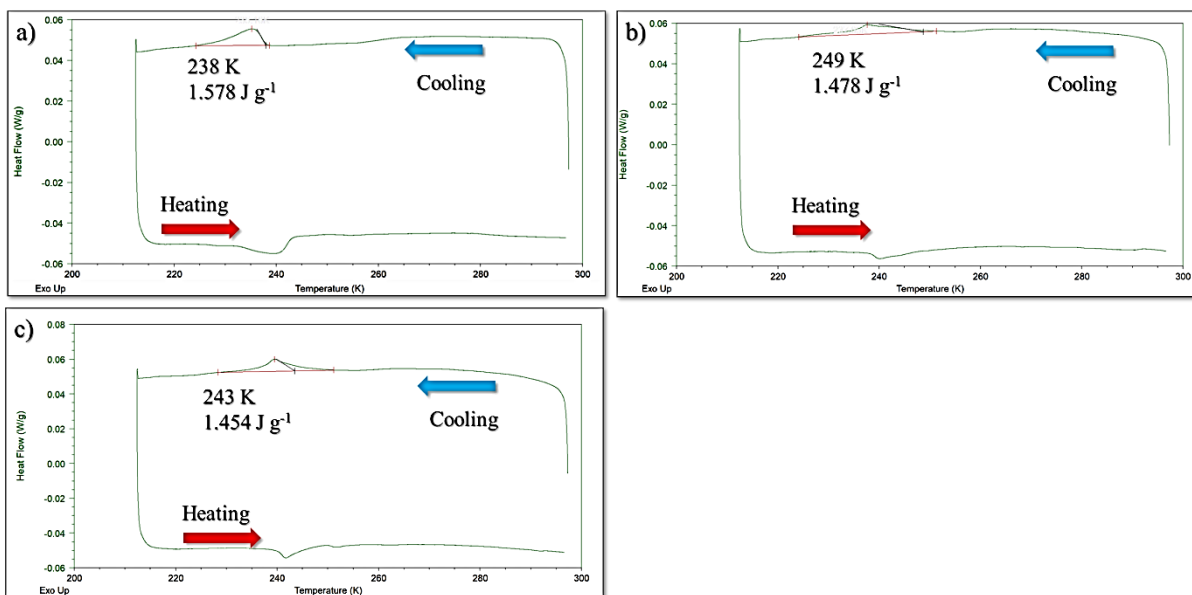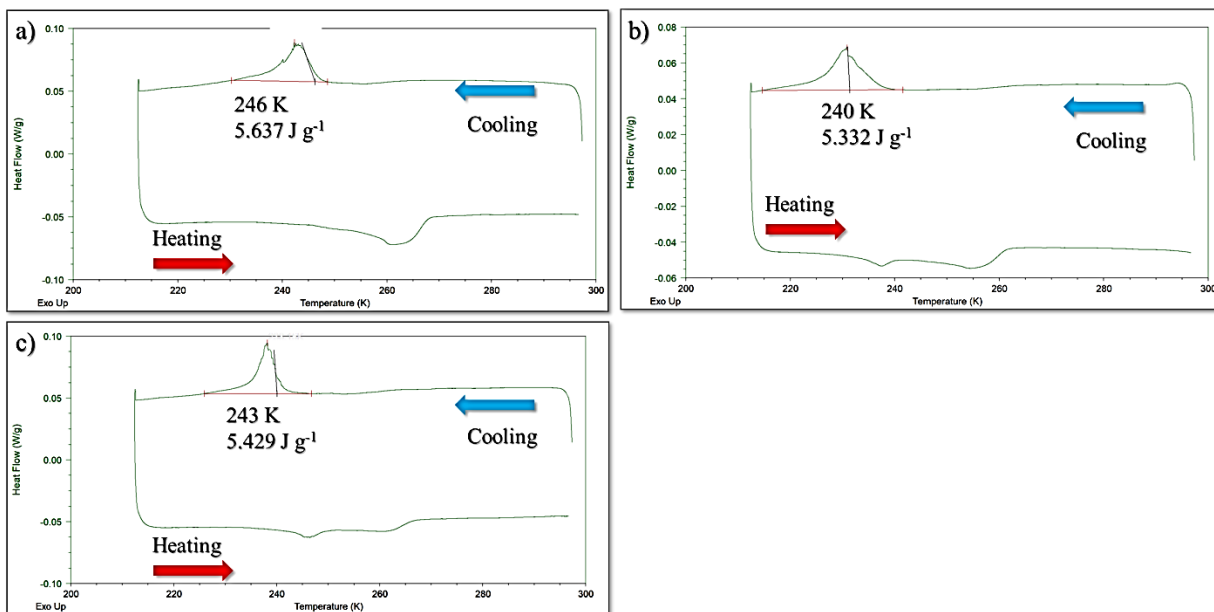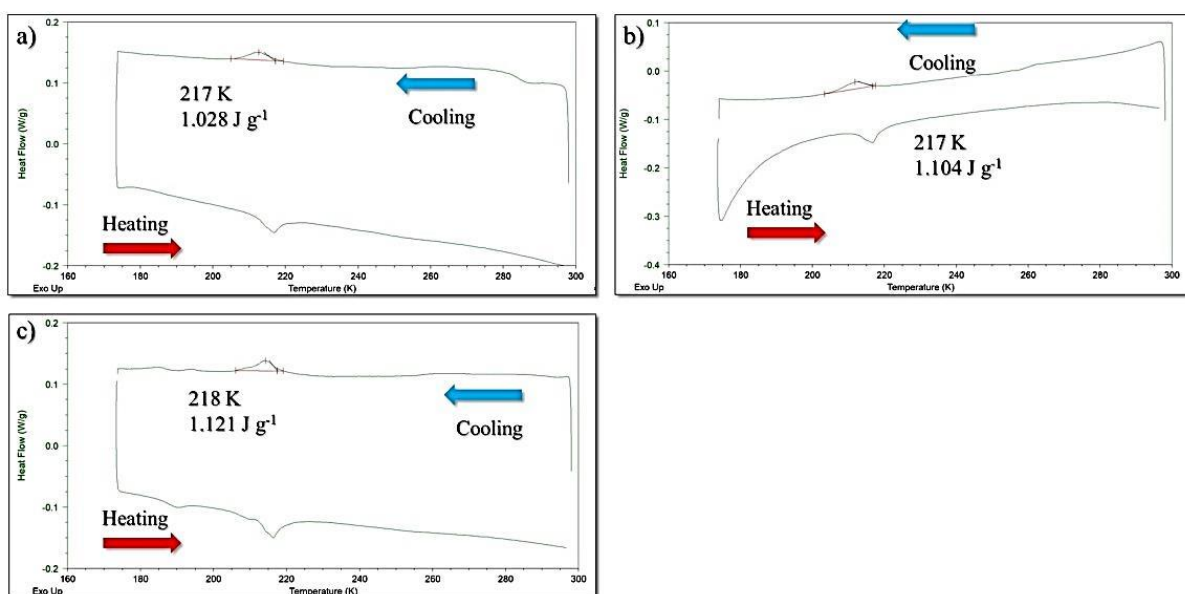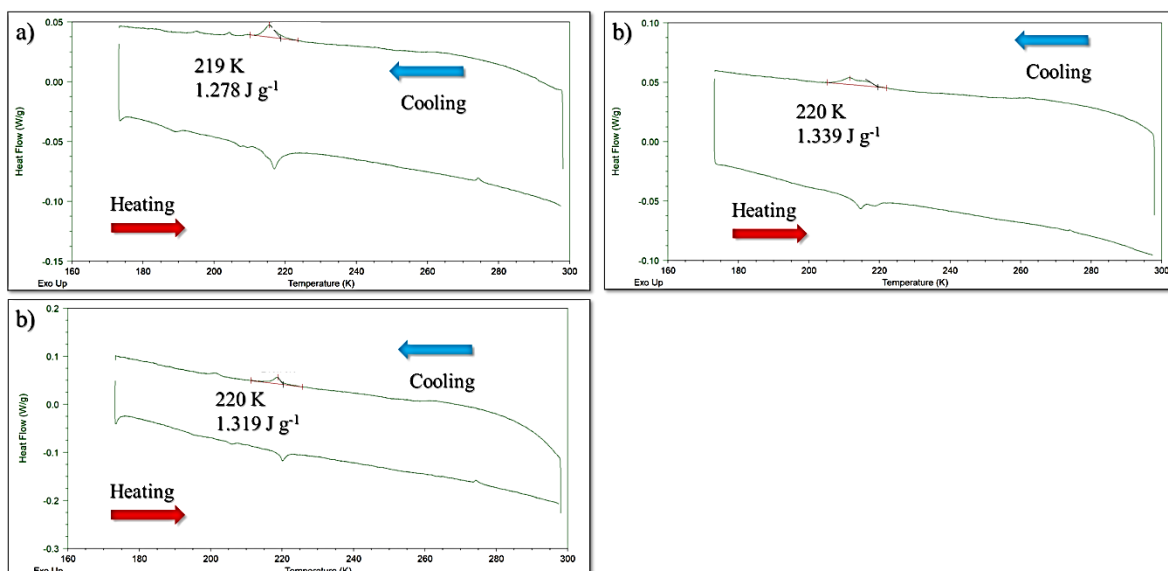
Figure S18: DSC thermograms for **ZnCP** cooled at 2 K min⁻¹. The onset temperature of the phase change and the peak integral are shown in each figure.
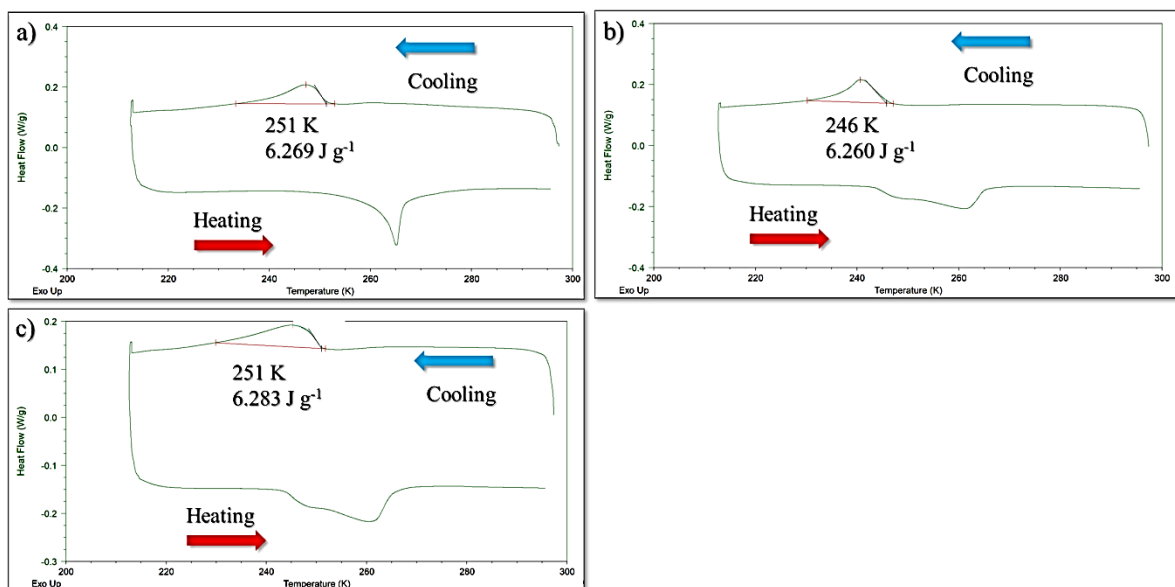
Figure S19: DSC thermograms for **NiCP** cooled at 5 K min⁻¹. The onset temperature of the phase change and the peak integral are shown in each figure.
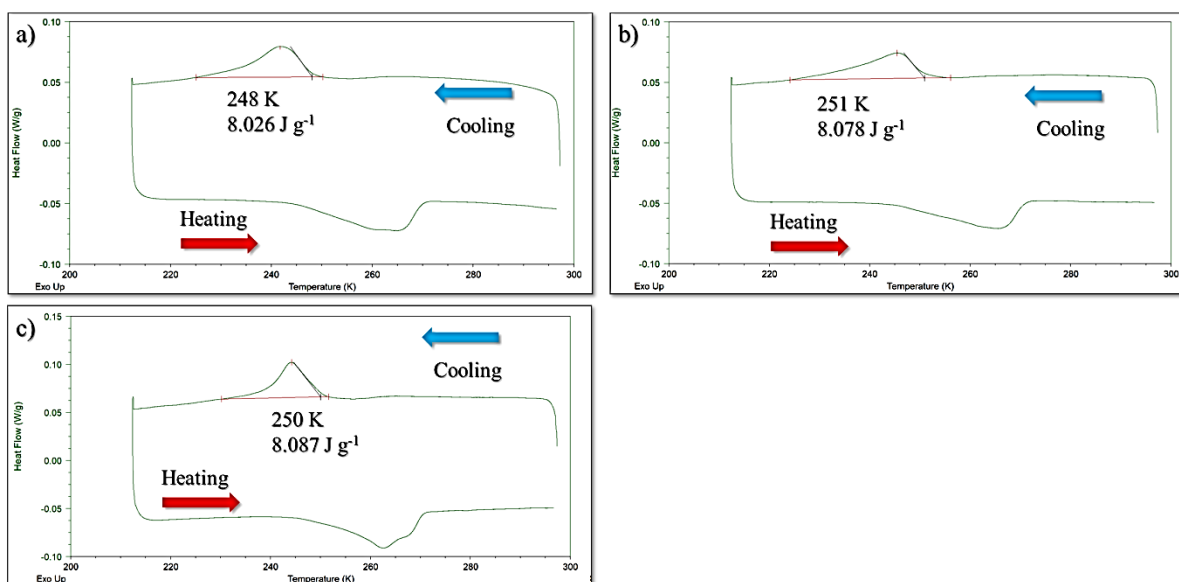
Figure S20: DSC thermograms for **NiCP** cooled at 2 K min^{-1}. The onset temperature of the phase change and the peak integral are shown in each figure.
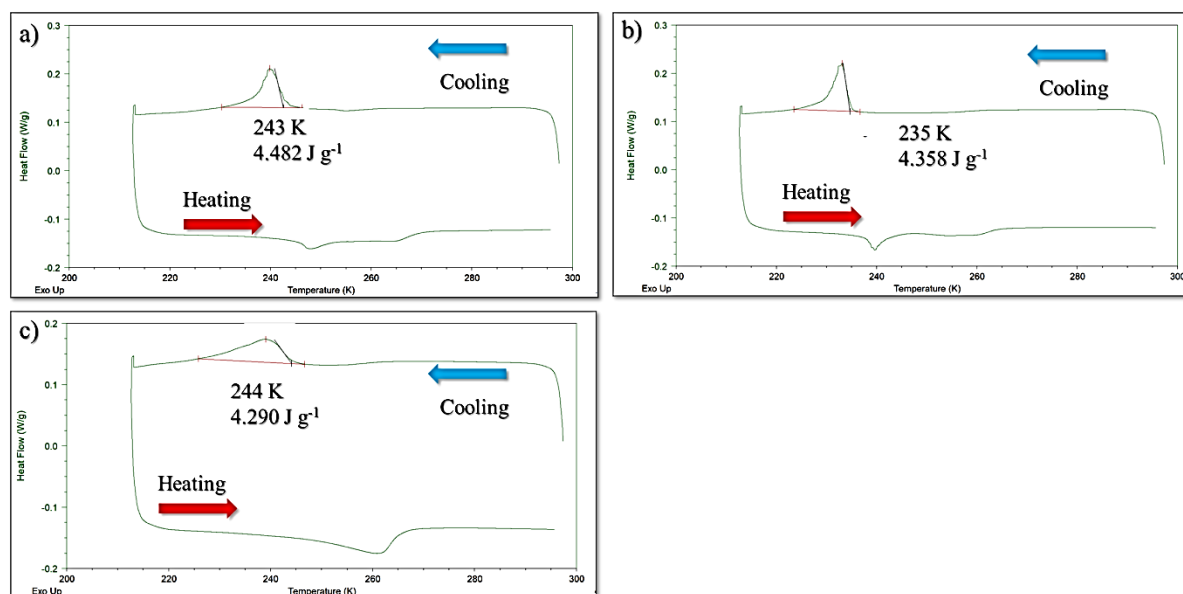
Figure S21: DSC thermograms for **CoCP** cooled at 5 K min^{-1}. The onset temperature of the phase change and the peak integral are shown in each figure.

Figure S22: DSC thermograms for **CoCP** cooled at 2 K min^{-1}. The onset temperature of the phase change and the peak integral are shown in each figure.

Figure S23: DSC thermograms for **CdCP** cooled at 5 K min^{-1}. The onset temperature of the phase change and the peak integral are shown in each figure.

Figure S24: DSC thermograms for **CdCP** cooled at 2 K min^{-1}. The onset temperature of the phase change and the peak integral are shown in each figure.

Table S15. Analysis of DSC data.

Material		Cooling at 5 K min^{-1}			Cooling at 2 K min^{-1}		
		Energy (J g^{-1})	Onset temperature (K)	Peak temperature (K)	Energy (J g^{-1})	Onset temperature (K)	Peak temperature (K)
ZnCP	Experiment 1	1.052	245	237	1.578	238	235
	Experiment 2	1.023	237	240	1.478	249	238
	Experiment 3	1.015	245	237	1.454	243	239
Average		1.030	242	238	1.503	243	237
Standard deviation		0.019	5	2	0.066	6	2
NiCP	Experiment 1	6.269	251	247	8.026	248	242
	Experiment 2	6.260	246	241	8.078	251	245
	Experiment 3	6.283	250	245	8.087	250	244
Average		6.271	249	244	8.064	250	244
Standard deviation		0.012	3	3	0.033	2	2
CoCP	Experiment 1	4.482	243	240	5.637	246	242
	Experiment 2	4.358	235	233	5.332	240	231
	Experiment 3	4.290	244	239	5.429	243	238
Average		4.377	241	237	5.466	243	237
Standard deviation		0.097	5	4	0.156	3	6
CdCP	Experiment 1	1.028	217	213	1.279	219	216
	Experiment 2	1.104	217	212	1.339	220	212
	Experiment 3	1.121	218	218	1.319	220	218
Average		1.084	217	213	1.312	220	215
Standard deviation		0.050	1	1	0.031	1	3

4. Principal Axis Strain (PAS) Calculations

The web-based tool PASCal[15] (Principal Axis Strain Calculator, http://pascal.chem.ox.ac.uk) was used to determine a set of principal axes and calculate the linear and volumetric coefficients of thermal expansion. The thermal expansion coefficients were calculated from the lattice parameters obtained from variable temperature single-crystal diffraction data.

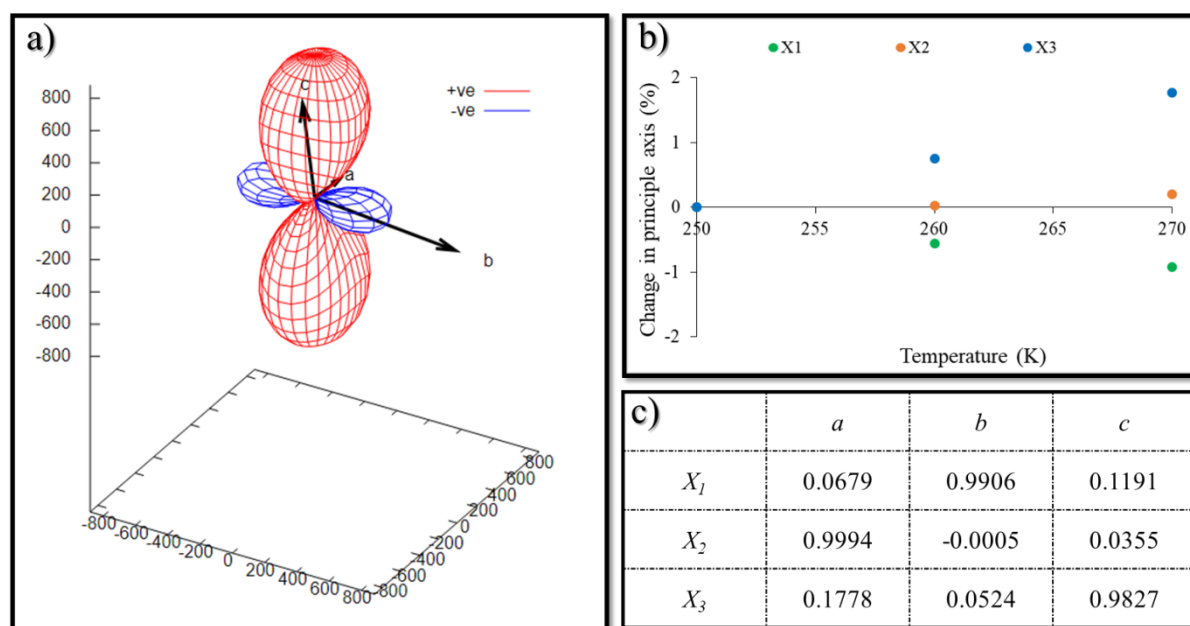## 4.1. Expansivity indicatrixes and transformation matrices of principal axes to unit-cell axes

Figure S25: Thermal expansion data for **ZnCP**^{HT} (250–270 K). The expansivity indicatrix is shown in **(a)**, while **(b)** illustrates the percentage change in the principal axes (relative to 250 K) as a function of temperature. The matrix relating the principal axes to the crystallographic axes is shown in **(c)**.
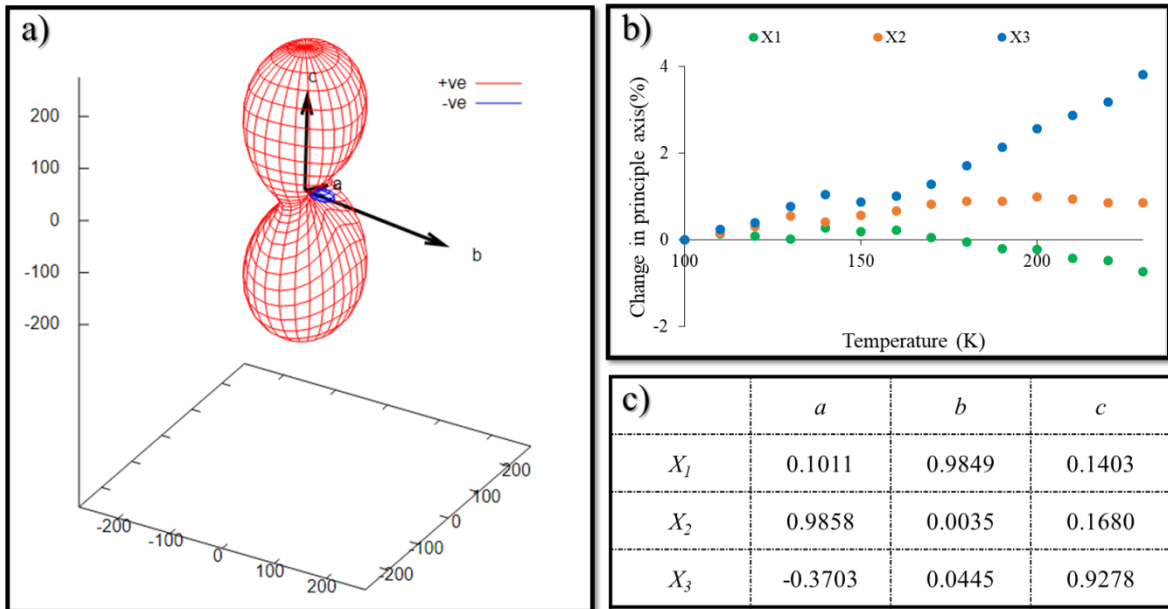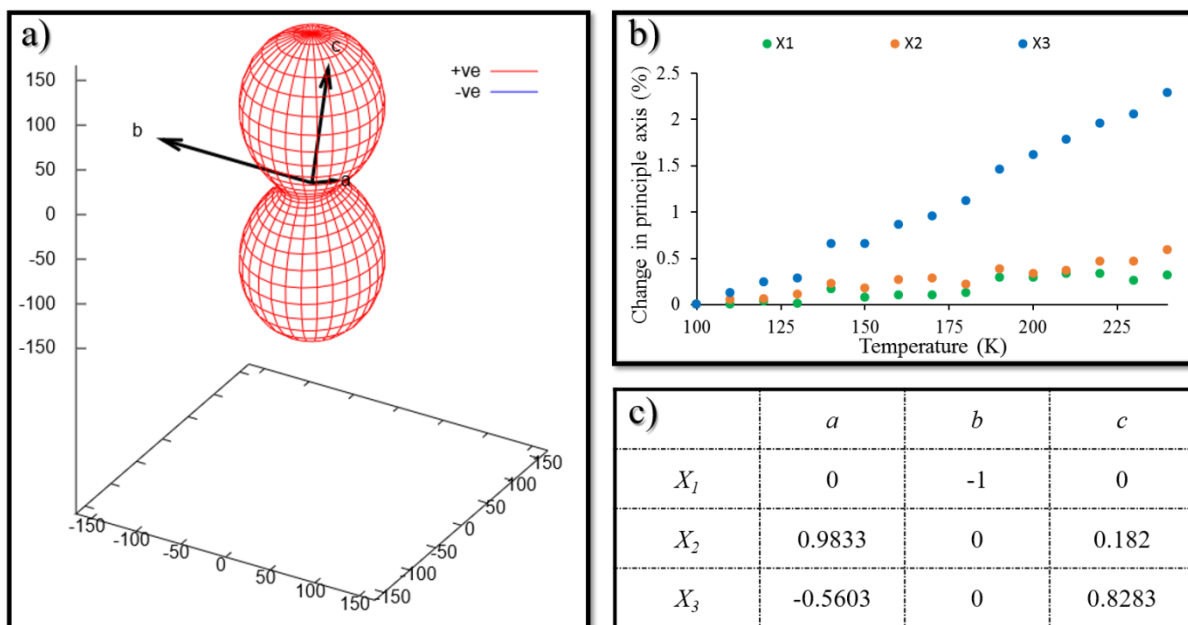
Figure S26: Thermal expansion data for ZnCP^{LT} (100–230 K). The expansivity indicatrix is shown in **(a)**, while **(b)** illustrates the percentage change in the principal axes (relative to 100 K) as a function of temperature. The matrix relating the principal axes to the crystallographic axes is shown in **(c)**.
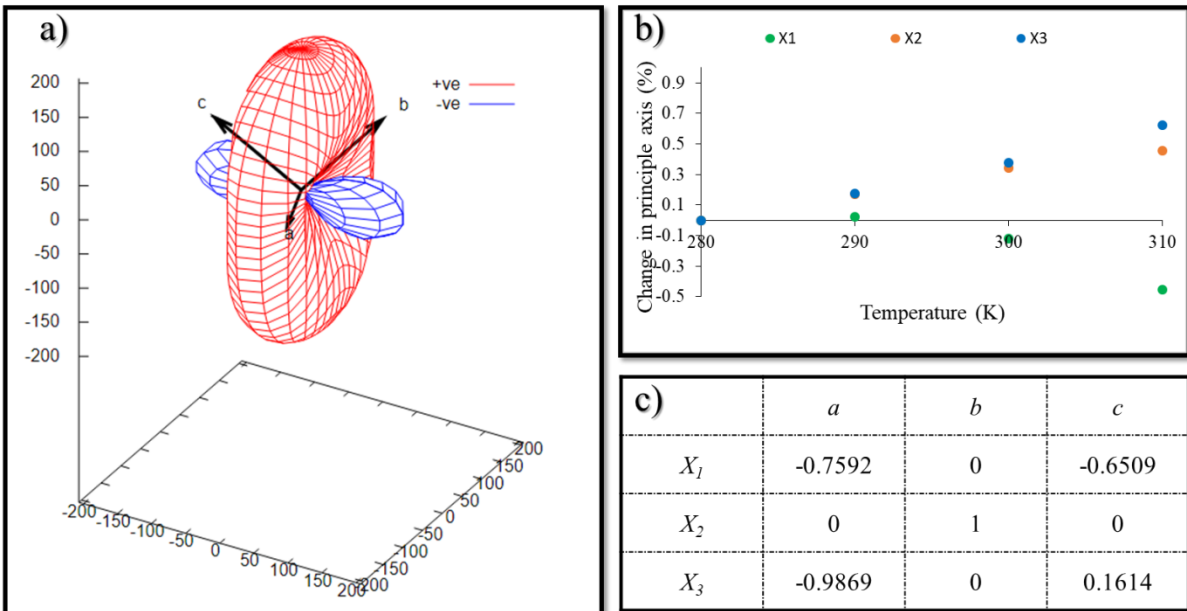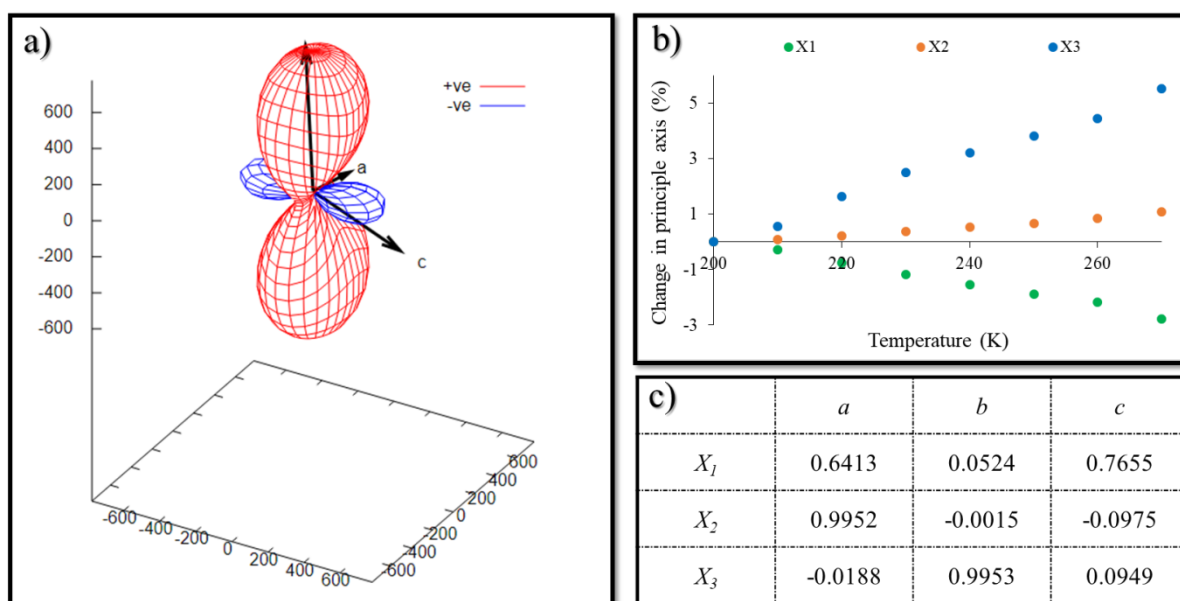

Figure S27: Thermal expansion data for CoCP^{HT} (280–310 K). The expansivity indicatrix is shown in **(a)**, while **(b)** illustrates the percentage change in the principal axes (relative to 280 K) as a function of temperature. The matrix relating the principal axes to the crystallographic axes is shown in **(c)**.
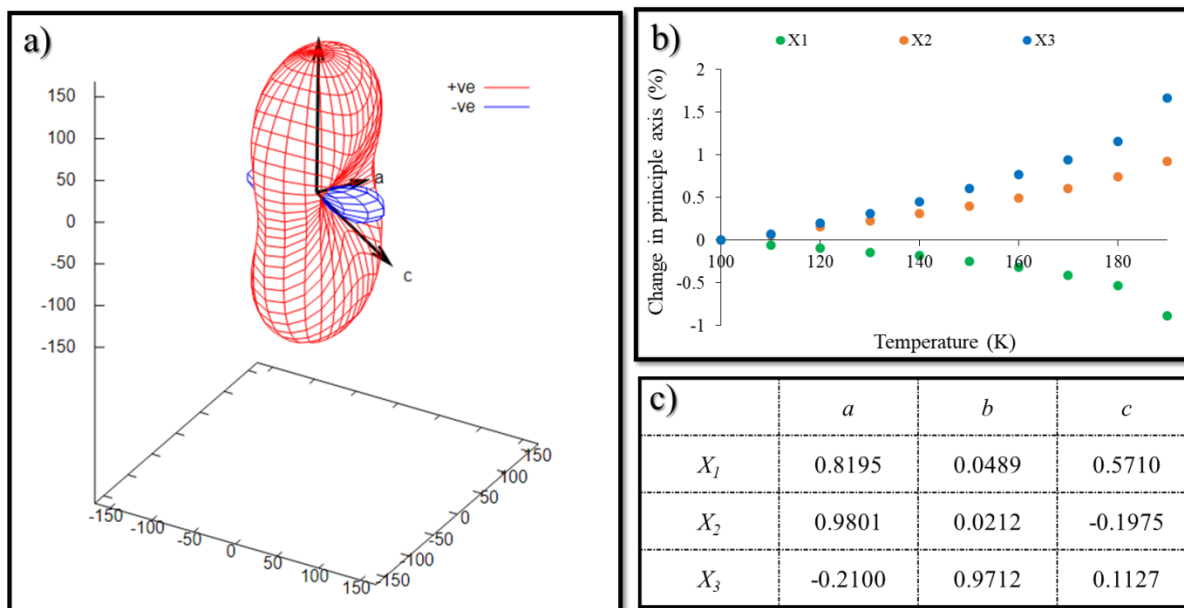
Figure S28: Thermal expansion data for **CoCP**[LT] (100–240 K). The expansivity indicatrix is shown in **(a)**, while **(b)** illustrates the percentage change in the principal axes (relative to 100 K) as a function of temperature. The matrix relating the principal axes to the crystallographic axes is shown in **(c)**.
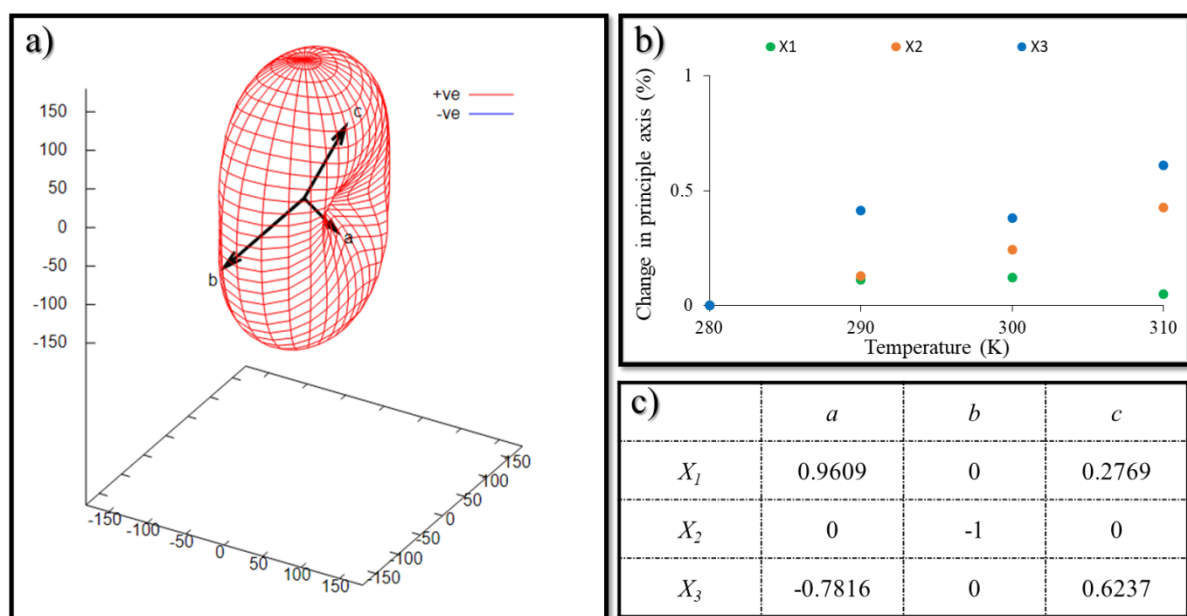

Figure S29: Thermal expansion data for **CdCP**[HT] (200–270 K). The expansivity indicatrix is shown in **(a)**, while **(b)** illustrates the percentage change in the principal axes (relative to 200 K) as a function of temperature. The matrix relating the principal axes to the crystallographic axes is shown in **(c)**.

Figure S30: Thermal expansion data for **CdCP**[LT] (100–190 K). The expansivity indicatrix is shown in **(a)**, while **(b)** illustrates the percentage change in the principal axes (relative to 100 K) as a function of temperature. The matrix relating the principal axes to the crystallographic axes is shown in **(c)**.

Table c):

	a	b	c
X_1	0.8195	0.0489	0.5710
X_2	0.9801	0.0212	-0.1975
X_3	-0.2100	0.9712	0.1127

Figure S31: Thermal expansion data for **NiCP**[HT] (280–310 K). The expansivity indicatrix is shown in **(a)**, while **(b)** illustrates the percentage change in the principal axes (relative to 280 K) as a function of temperature. The matrix relating the principal axes to the crystallographic axes is shown in **(c)**.

Table c):

	a	b	c
X_1	0.9609	0	0.2769
X_2	0	-1	0
X_3	-0.7816	0	0.6237
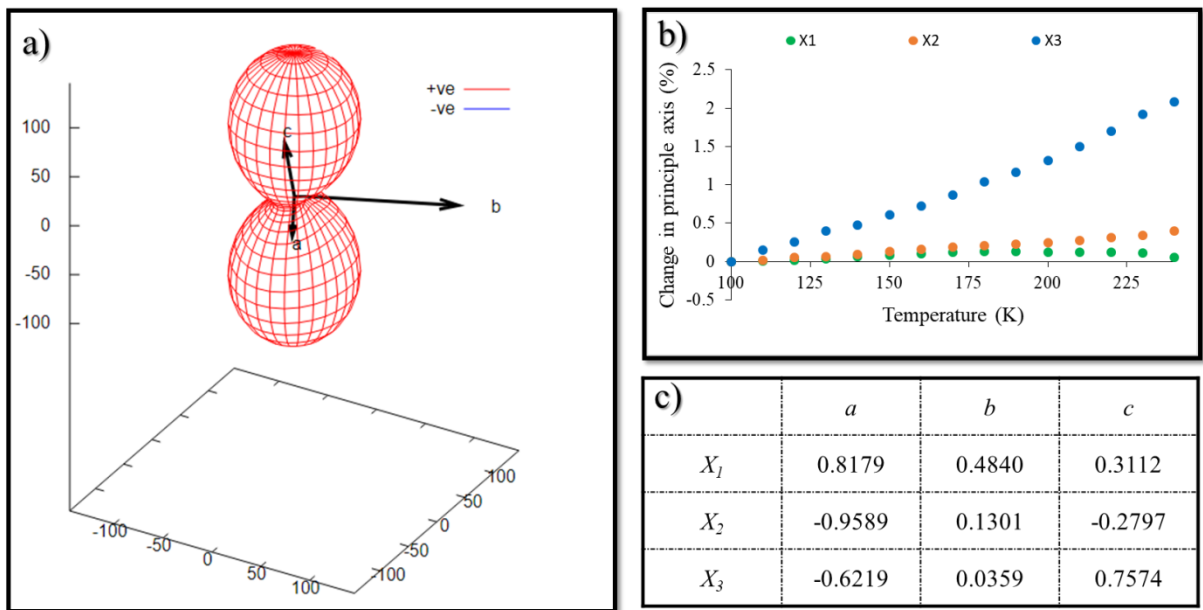
Figure S32: Thermal expansion data for **NiCP^{LT}** (100–240 K). The expansivity indicatrix is shown in **(a)**, while **(b)** illustrates the percentage change in the principal axes (relative to 100 K) as a function of temperature. The matrix relating the principal axes to the crystallographic axes is shown in **(c)**.

c)	a	b	c
X_1	0.8179	0.4840	0.3112
X_2	-0.9589	0.1301	-0.2797
X_3	-0.6219	0.0359	0.7574
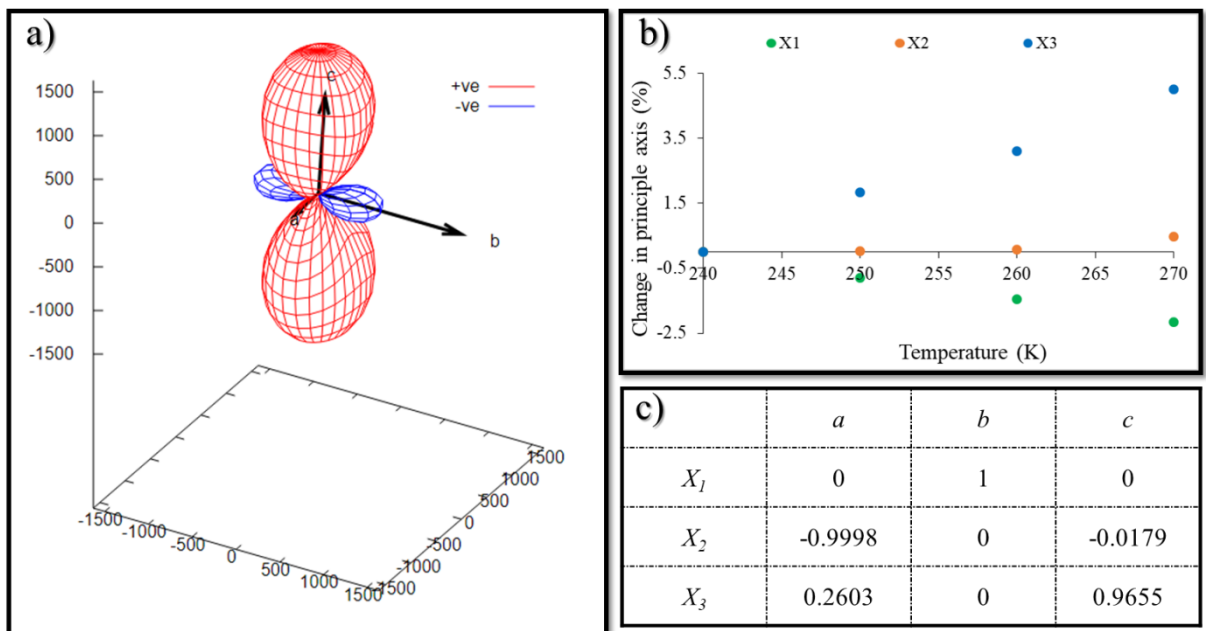
Figure S33: Thermal expansion data for **ZnCoCP^{HT}** (240–270 K). The expansivity indicatrix is shown in **(a)**, while **(b)** illustrates the percentage change in the principal axes (relative to 240 K) as a function of temperature. The matrix relating the principal axes to the crystallographic axes is shown in **(c)**.
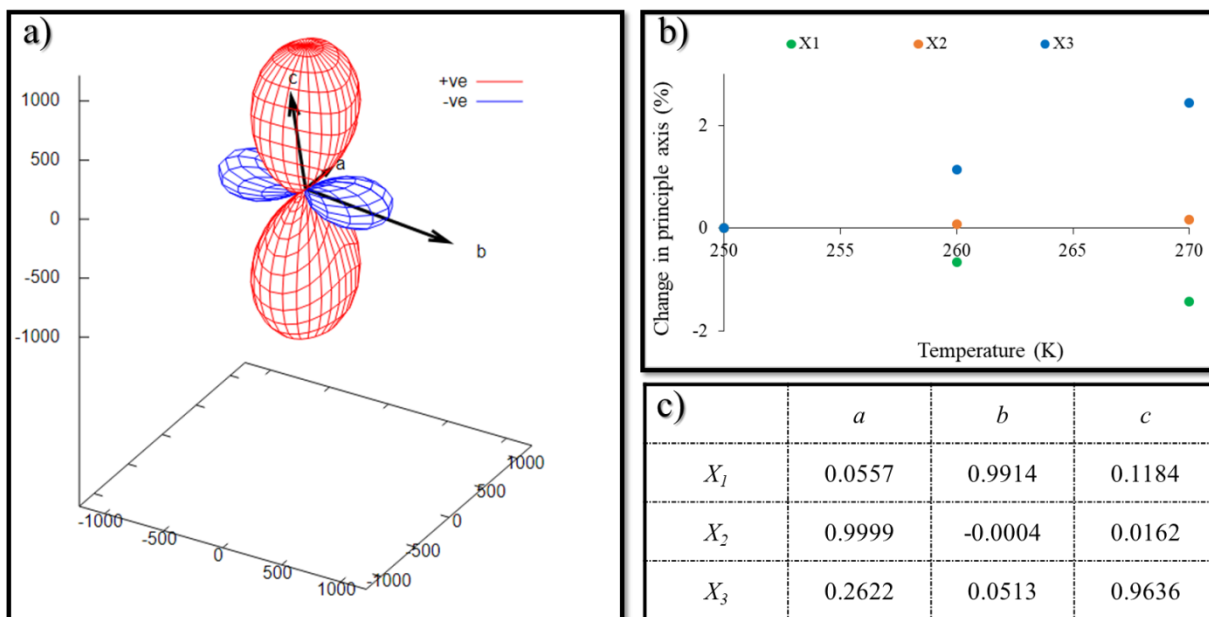
c)	a	b	c
X_1	0	1	0
X_2	-0.9998	0	-0.0179
X_3	0.2603	0	0.9655
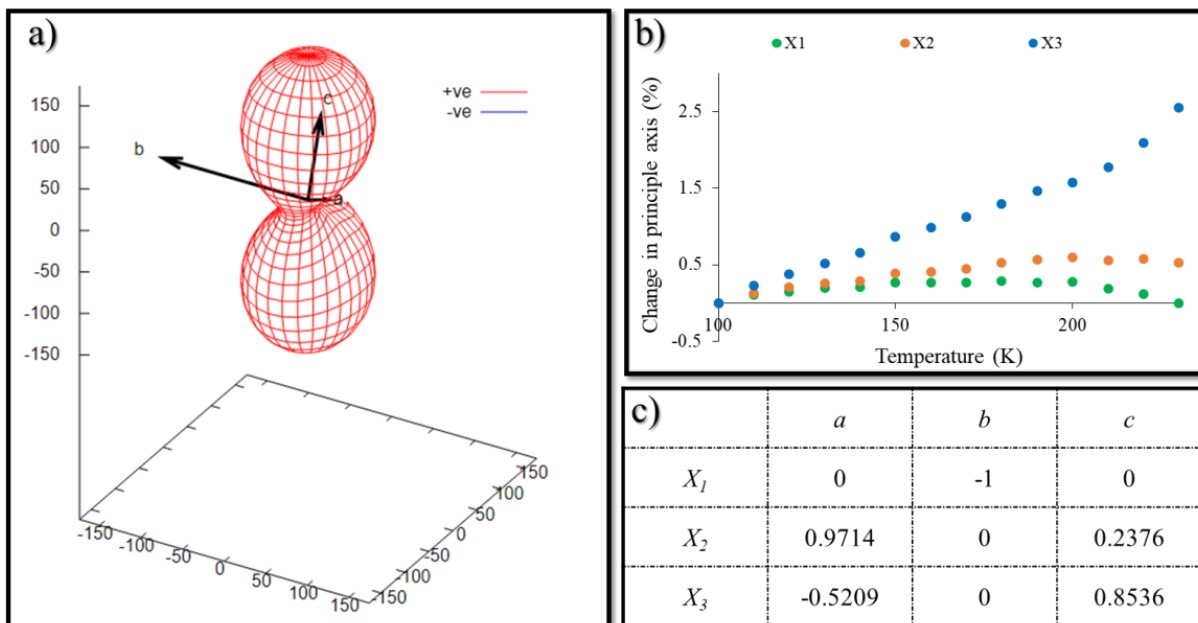
Figure S34: Thermal expansion data for **ZnCoCP^{LT}** (100–230 K). The expansivity indicatrix is shown in **(a)**, while **(b)** illustrates the percentage change in the principal axes (relative to 100 K) as a function of temperature. The matrix relating the principal axes to the crystallographic axes is shown in **(c)**.
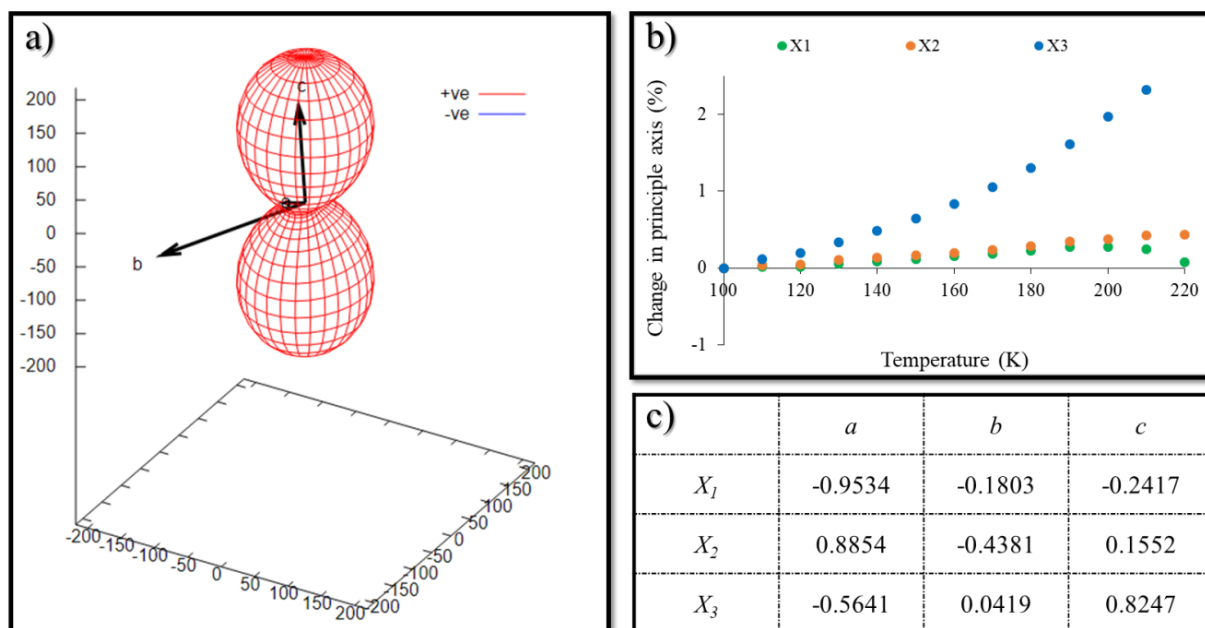

Figure S35: Thermal expansion data for **ZnCdCP^{HT}** (250–270 K). The expansivity indicatrix is shown in **(a)**, while **(b)** illustrates the percentage change in the principal axes (relative to 250 K) as a function of temperature. The matrix relating the principal axes to the crystallographic axes is shown in **(c)**.
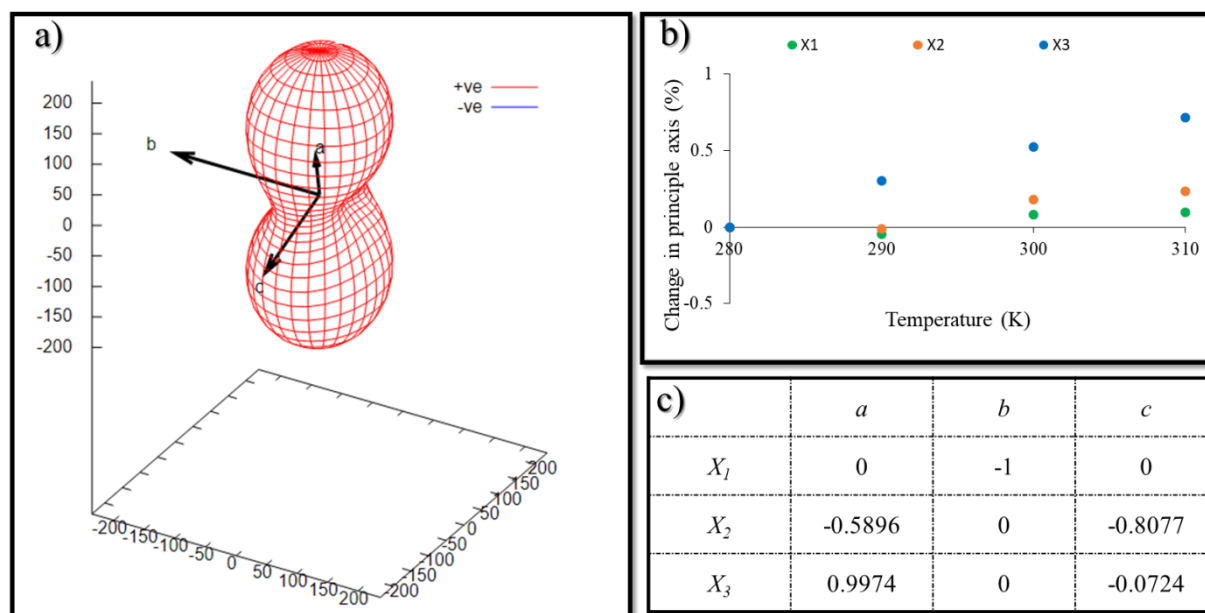
Figure S36: Thermal expansion data for **ZnCdCP^{LT}** (100–230 K). The expansivity indicatrix is shown in **(a)**, while **(b)** illustrates the percentage change in the principal axes (relative to 100 K) as a function of temperature. The matrix relating the principal axes to the crystallographic axes is shown in **(c)**.

Table (c) for Figure S36:

	a	b	c
X_1	-0.9534	-0.1803	-0.2417
X_2	0.8854	-0.4381	0.1552
X_3	-0.5641	0.0419	0.8247

Figure S37: Thermal expansion data for **NiCdCP^{HT}** (280–310 K). The expansivity indicatrix is shown in **(a)**, while **(b)** illustrates the percentage change in the principal axes (relative to 280 K) as a function of temperature. The matrix relating the principal axes to the crystallographic axes is shown in **(c)**.

Table (c) for Figure S37:

	a	b	c
X_1	0	-1	0
X_2	-0.5896	0	-0.8077
X_3	0.9974	0	-0.0724
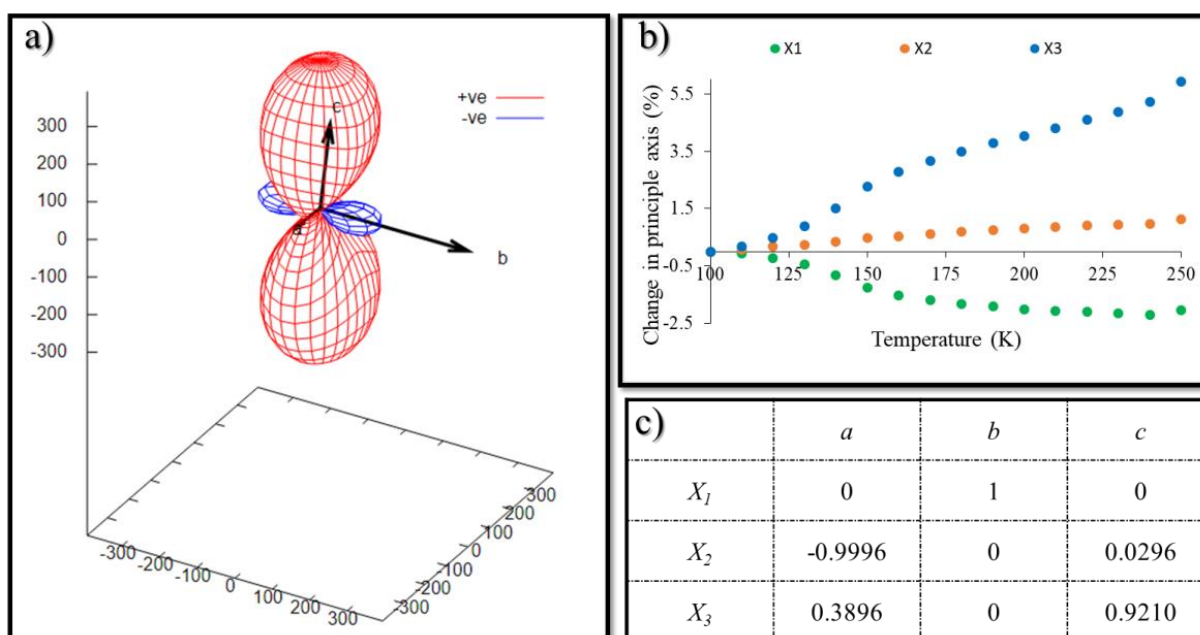
Figure S38: Thermal expansion data for **NiCdCP**[LT] (100–250 K). The expansivity indicatrix is shown in **(a)**, while **(b)** illustrates the percentage change in the principal axes (relative to 100 K) as a function of temperature. The matrix relating the principal axes to the crystallographic axes is shown in **(c)**.

4.2. Transformation to comparable principal axes

Although principal axes are generated automatically by PasCAL, the authors determined that the inconsistent assignment of these axes inhibited direct comparison of the thermal expansion properties of the CPs. Therefore, an alternative set of principal axes (denoted *Y1*, *Y2* and *Y3*) was determined for each CP so that the principal axes for all forms can be compared more directly to one another. Accordingly, the linear thermal expansion coefficients are also denoted α_{Y1}, α_{Y2} and α_{Y3}.

ZnCP[HT]	a	b	c
Y_1	-0.9994	0.0005	-0.0355
Y_2	0.0679	0.9906	0.1191
Y_3	0.1778	0.0524	0.9827

ZnCP[LT]	a	b	c
Y_1	-0.9858	-0.0035	-0.1680
Y_2	0.1011	0.9849	0.1403
Y_3	-0.3703	0.0445	0.9278

NiCP[HT]	a	b	c
Y_1	0.9609	0	0.2769
Y_2	0	-1	0
Y_3	-0.7816	0	0.6237

NiCP[LT]	a	b	c
Y_1	0.9512	-0.1301	0.2798
Y_2	0.8179	0.4840	0.3112
Y_3	-0.6519	0.0359	0.7574

CoCP[HT]	a	b	c
Y_1	-0.9869	0	0.1614
Y_2	0	1	0
Y_3	0.7592	0	0.6509

CoCP[LT]	a	b	c
Y_1	0.9833	0	0.182
Y_2	0	1	0
Y_3	-0.5603	0	0.8283

CdCP[HT]	a	b	c
Y_1	-0.9952	0.0015	0.0975
Y_2	0.0188	-0.9953	-0.0949
Y_3	0.6413	0.0524	0.7655

CdCP[LT]	a	b	c
Y_1	-0.9801	-0.0212	0.1975
Y_2	0.2100	-0.9712	-0.1127
Y_3	0.8195	0.0489	0.5710

ZnCoCP[HT]	a	b	c
Y_1	0.9998	0	0.0179
Y_2	0	1	0
Y_3	0.2603	0	0.9655

ZnCoCP[LT]	a	b	c
Y_1	0.9714	0	0.2376
Y_2	0	1	0
Y_3	-0.5209	0	0.8536

NiCdCP[HT]	a	b	c
Y_1	0.9974	0	-0.0724
Y_2	0	1	0
Y_3	0.5896	0	0.8077

NiCdCP[LT]	a	b	c
Y_1	0.9996	0	-0.0296
Y_2	0	1	0
Y_3	0.3896	0	0.9210

ZnCdCP[HT]	a	b	c
Y_1	-0.9999	0.0004	-0.0162
Y_2	0.0557	0.9914	0.1184
Y_3	0.2622	0.0513	0.9636

ZnCdCP[LT]	a	b	c
Y_1	-0.9534	-0.1803	-0.2417
Y_2	0.8854	-0.4381	0.1552
Y_3	-0.5641	0.0419	0.8247

Figure S39: Transformed matrices for the principal axes of each CP and their individual forms

Table S16. Summary of the thermal expansion coefficients for the materials studied.

Material	α_{Y1} (MK^{-1})	α_{Y2} (MK^{-1})	α_{Y3} (MK^{-1})	α_V (MK^{-1})
ZnCP^{HT}	100(18)	−462(23)	882(32)	575(81)
ZnCP^{LT}	69(10)	−57(13)	275(16)	292(10)
NiCP^{HT}*	16(20)	140(7)	180(30)	371(36)
NiCP^{LT}	27(1)	8(2)	146(5)	182(3)
CoCP^{HT}*	207(7)	153(7)	−150(40)	239(36)
CoCP^{LT}	37(2)	26(2)	168(4)	237(6)
CdCP^{HT}	154(8)	778(19)	−389(11)	531(12)
CdCP^{LT}	98(6)	169(18)	−81(14)	189(10)
ZnCoCP^{HT}	152(43)	−712(11)	1632(36)	1070(60)
ZnCoCP^{LT}	42(6)	3(8)	176(10)	224(9)
ZnCdCP^{HT}	81(1)	−711(14)	1216(19)	571(3)
ZnCdCP^{LT}	20(6)	38(1)	218(15)	285(12)
NiCdCP^{HT}*	236(13)	42(11)	89(13)	378(24)
NiCdCP^{LT}	73(3)	−160(16)	394(11)	306(16)

*Data determined by means of solvent cell (temperature range 280–310 K)
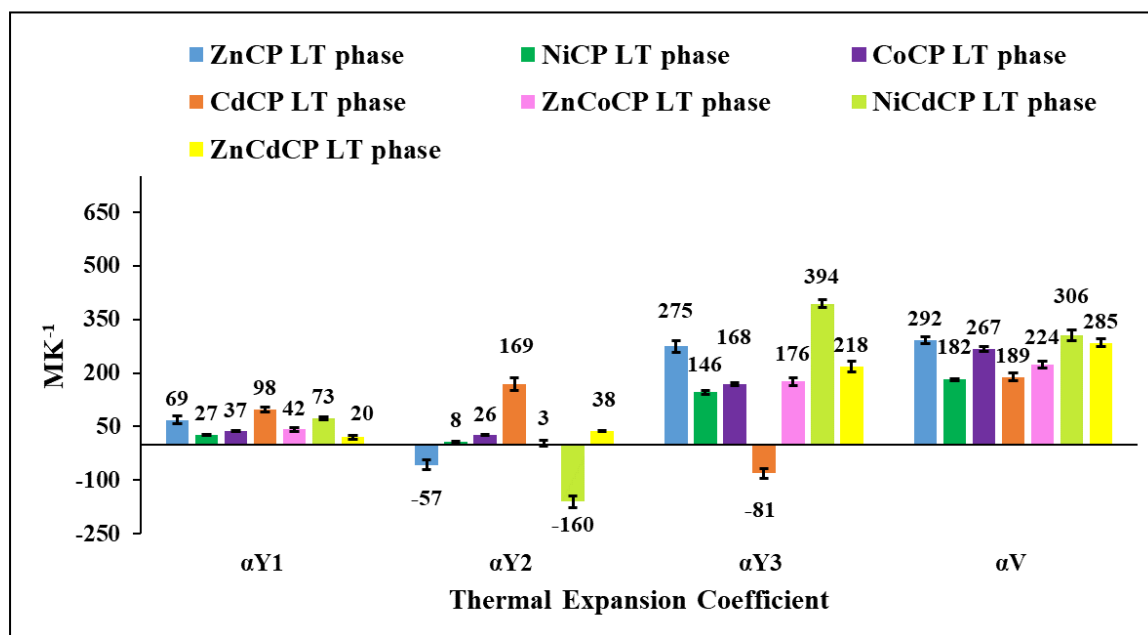
Figure S40: Thermal expansion coefficients determined for the low temperature phases of the CP series. Error bars and specific values are indicated.

Table S17. Reported extreme and/or anisotropic coefficients of thermal expansion

Material		Temperature range (K)	α_{Y1} (MK^{-1})	α_{Y2} (MK^{-1})	α_{Y3} (MK^{-1})	α_V (MK^{-1})	Reference
Organic materials	IMD-HBC	100–360	-115	18	210	110	16
	(S,S)-octa-3,5-diyn-2,7-diol	225–330	515	-85	-204	47	17
	18C6N	90–273	-129(15)	144(14)	282(16)	311(17)	18
	$C_{12}H_{24}O_6 \cdot 2CH_3NO_2$	180–273	-198(12)	215(16)	369(20)	378(22)	19
	$CD_3OD \cdot D_2O$	20–155	-64(4)	462(4)	93(4)	494(6)	20
	β L-PGA	320–420	-54.5(8)	303(1)	-3.62(8)	245(2)	21
	CA-Pyz	250–300	-1375(30)	196(30)	1524(30)	245(30)	22
Metal-organic frameworks	[Zn$_2$(fu-L^1)$_2$dabco]n	303–463	-380	1161	14.6	837	23
	[Zn$_2$(fu-L^2)$_2$dabco]n	303–463	-186	674	17.1	524	23
	[Fe$_{0.84}$Ni$_{0.16}$(bpac)(Au(CN)$_2$)$_2$]·2EtOH	160–215	-3200	5200	1500	3200	24
	α-Cu(tcm)	20–240	591(28)	-407(28)	-13.6(11)	-*	25
	FJI-H11-Me	100–300	-37.8(2)	=X1	653.2(5)	568.1(7)	26
	FJI-H11-Me	100–300	-33.2(3)	=X1	489.4(10)	416.8(11)	26
	[Cd(34pba)(44pba)]	112–300	61(1)	482(12)	-218(3)	319(13)	27
	{[FeTp(CN)$_3$]$_2$Co-(Bib)$_2$ }·5H$_2$O	300–350	-656	-18	197	-489	28
	{[FeTp(CN)$_3$]$_2$Co-(Bib)$_2$ }·5H$_2$O	180–240	85	278	1089	1498	28
1D coordination polymers	[ZnCl$_2$(μ-bipy)]$_\infty$ 1D-α	170–295	1(2)	36(3)	92(7)	134(7)	29
	[ZnCl$_2$(μ-bipy)]$_\infty$ 1D-β	155.5–295	-10(3)	39(3)	77(2)	108(3)	29
	Ag[AuCl$_2$(CN)$_2$]	100–300	49.4(13)	23.6(10)	-4.7(14)	88(3)	30
	Ag[AuBr$_2$(CN)$_2$]	100–300	52.1(9)	25.3(6)	5.1(5)	97.7(9)	30
	Cu[AuBr$_2$(CN)$_2$]	100–300	45.9(5)	-11.3(2)	73.6(6)	103.1(12)	30
	[Cu$_3$(cdm)$_4$]	120–350	-18.8(6)	=X1	46.8(19)	9.3(9)	31
Other	Ag$_3$[Co(CN)$_6$]	20–300	150	=X1	-130	-*	32
	[Ag(en)]NO$_3$-I	120–360	-89.7(15)	37.9(12)	149.2(12)	95.8(20)	33
	(Mn$_{0.95}$Ni$_{0.05}$)CoGe	270–320	-1804(105)	1265(71)	46(2)	-621(35)	34

*Value not reported

5. Powder X-ray diffraction (PXRD)

A Bruker D2 Phaser diffractometer was used to determine experimental diffractograms. The diffractometer utilises Bragg-Brentano geometry and Cu Kα radiation (λ = 1.5418 Å) as the incident beam. The diffractometer was operated at 30 kV and 10 mA. Intensity data were recorded with a Lynxeye detector using a rotating flat stage (30° min^{-1}). Samples were loaded onto a zero-background sample holder and levelled with a glass slide. The diffractograms were determined under ambient conditions with a scanning range of 5–35°, a step size of 0.016° and a 0.8 second scan speed. Slight shifts between the simulated (from 270 K data) and the experimental (ambient temperature) diffractograms are related to thermal expansion of the materials. Further changes in peak position and intensity may be attributed to preferred orientation since it was not possible to grind the samples prior to measurement owing to labile desolvation behaviour. To aid comparison an enhanced view (data truncated along the ordinate) of the simulated diffractogram has also been included in the following figures.
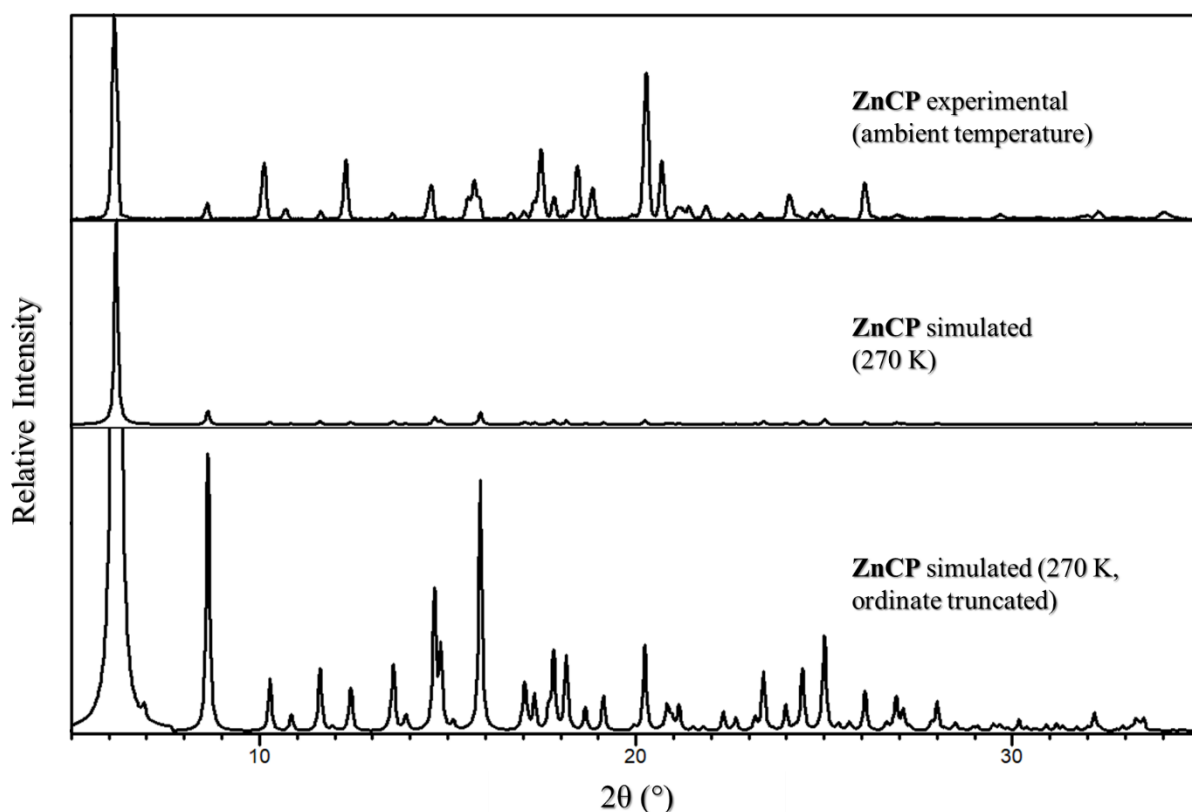
Figure S41: Simulated and experimental diffractograms for ZnCP^{HT}.
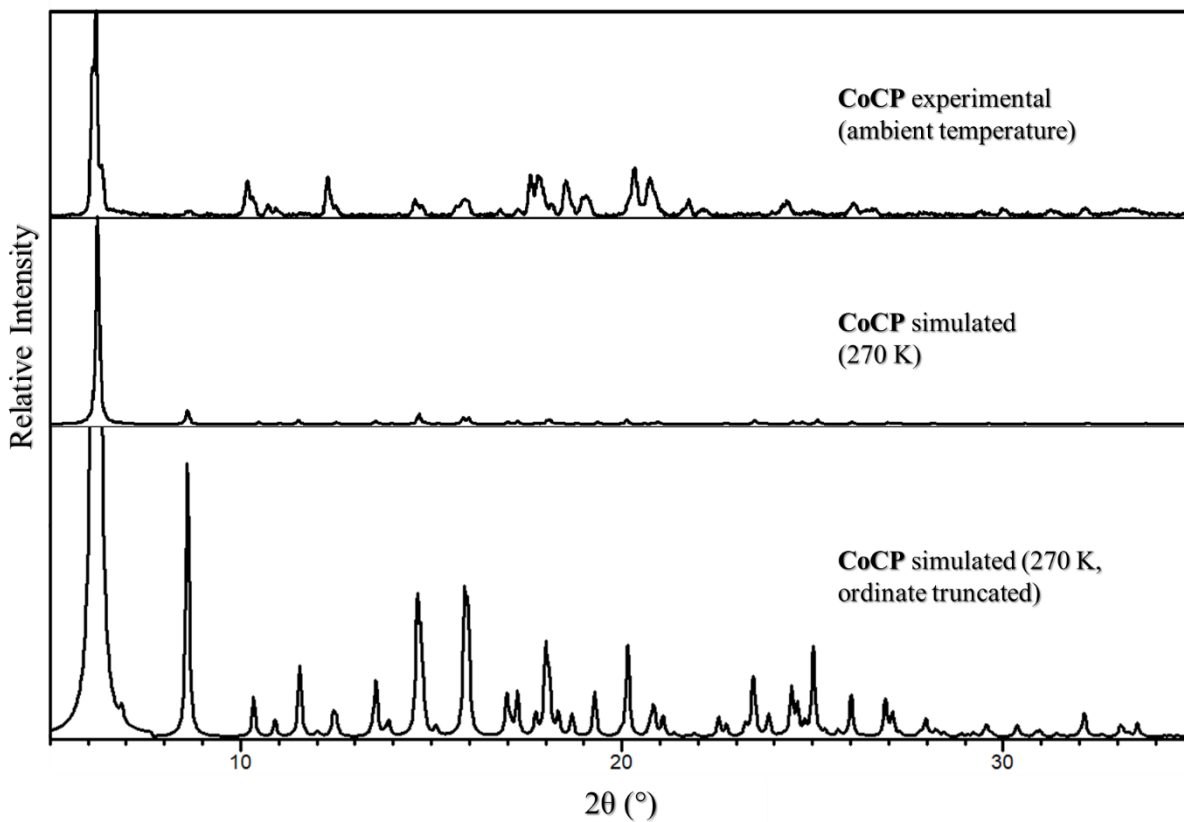
Figure S42: Simulated and experimental diffractograms for CoCP^HT.
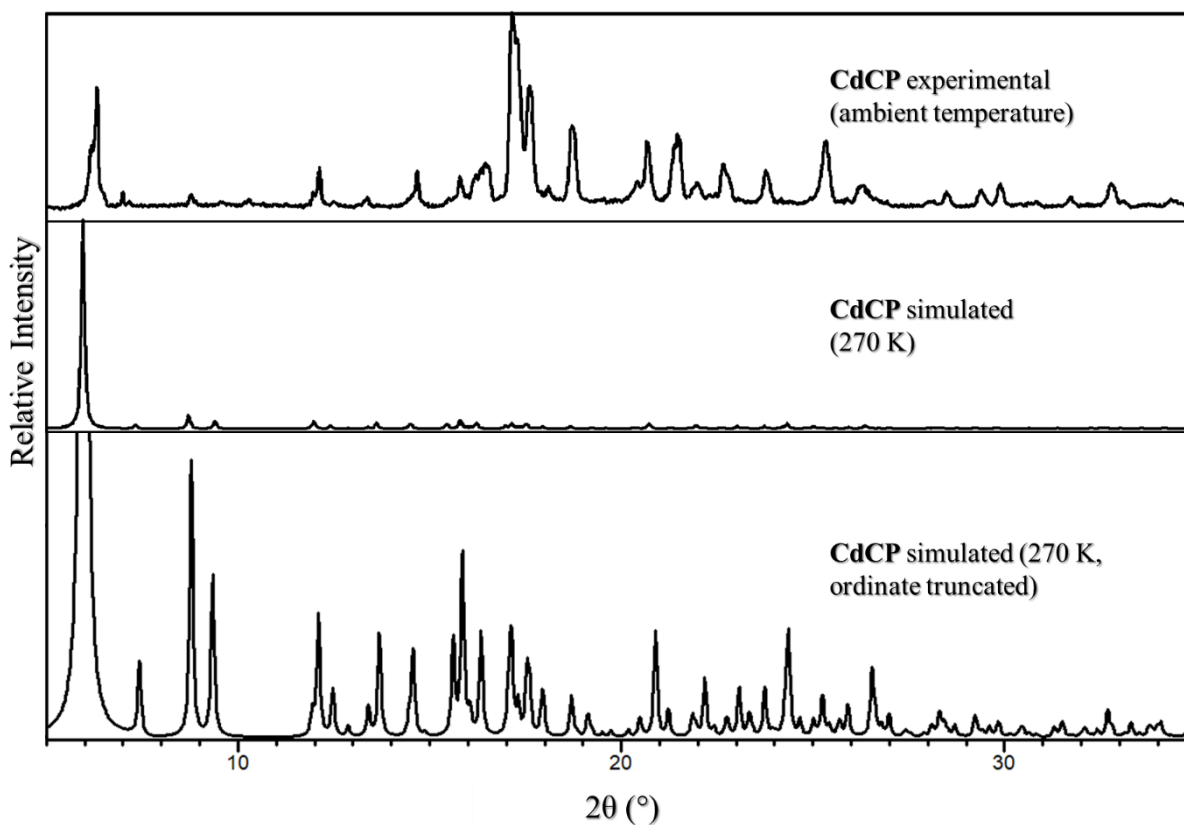
Figure S43: Simulated and experimental diffractograms for CdCP^HT.
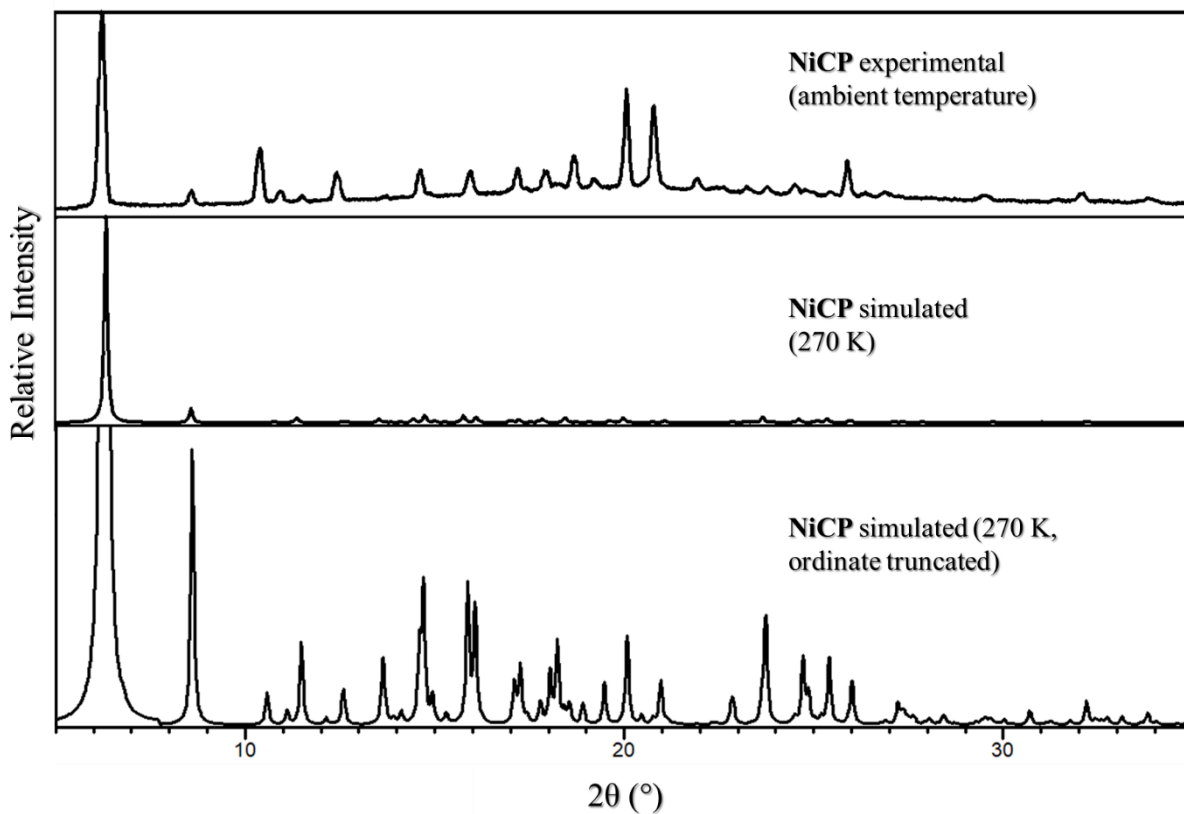
Figure S44: Simulated and experimental diffractograms for NiCP^HT.
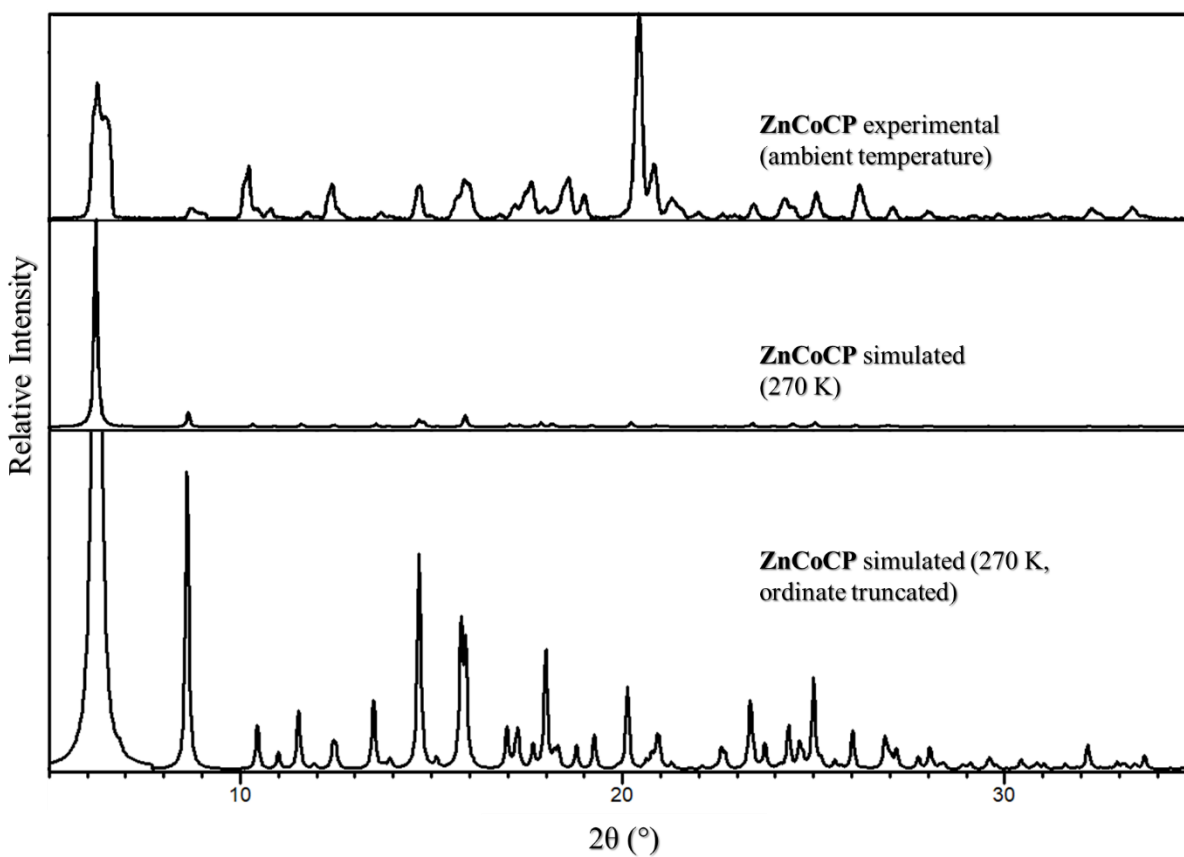
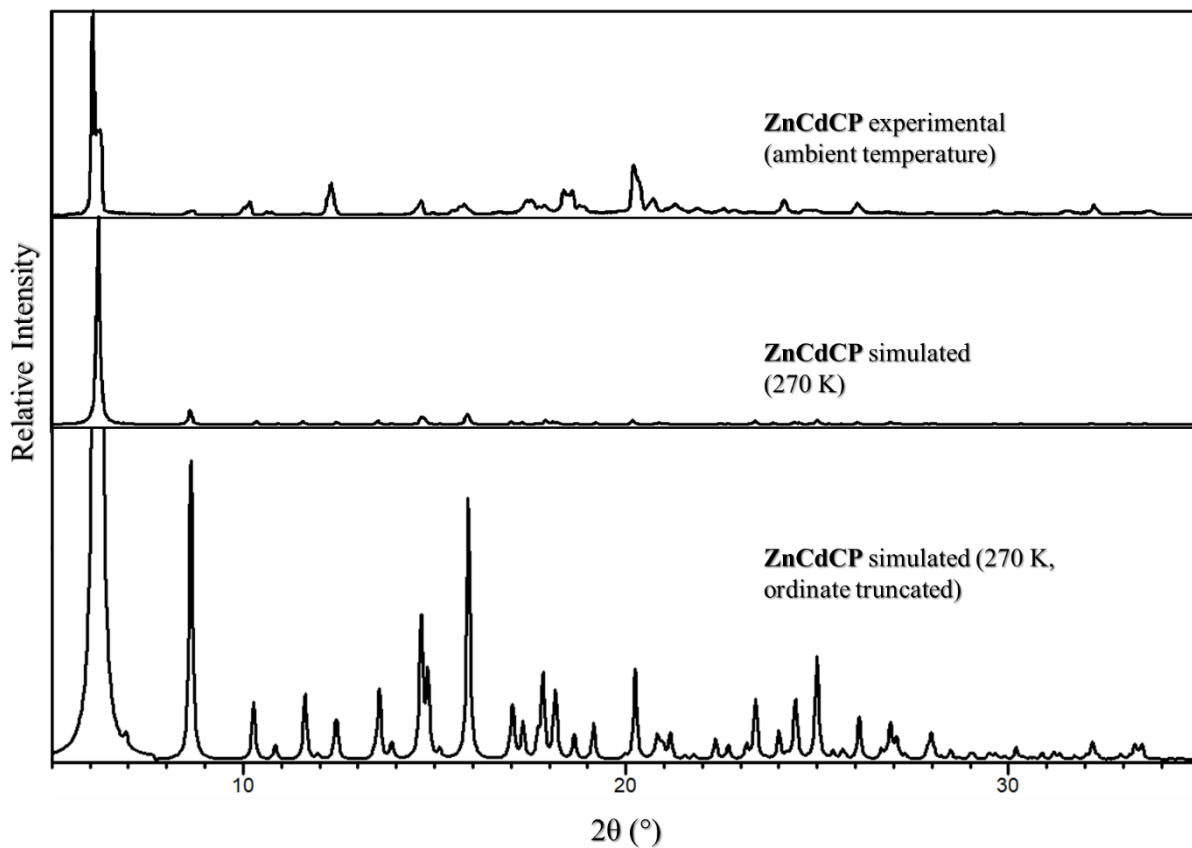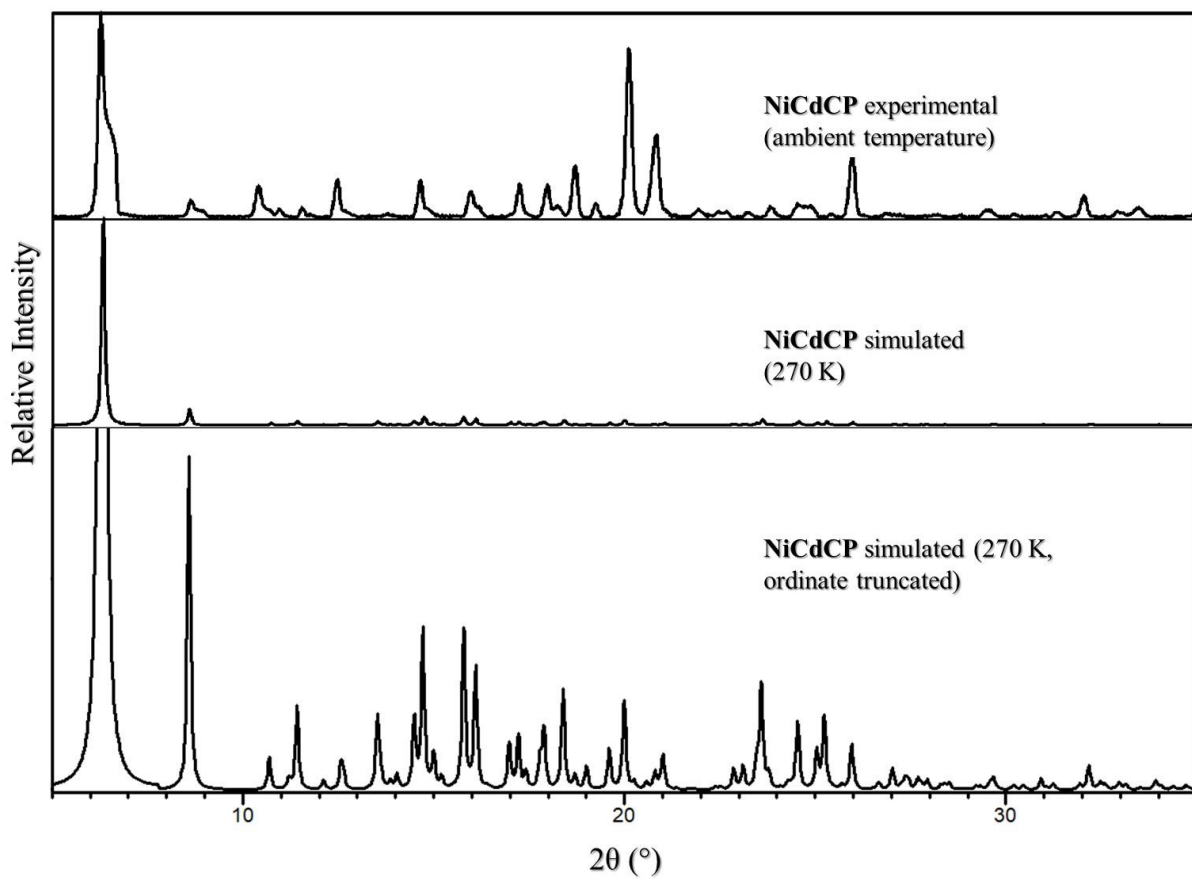**Figure S45:** Simulated and experimental diffractograms for ZnCoCP^HT.

Figure S46: Simulated and experimental diffractograms for ZnCdCP[HT].

Figure S47: Simulated and experimental diffractograms for NiCdCP[HT].

6. Fourier-transform infrared spectrophotometry (FT-IR)

IR spectra were recorded using a Bruker Alpha P ATR-IR instrument. A background measurement was performed before each spectrum was recorded. Samples were briefly dried on filter paper before measurement to remove any surface solvent.
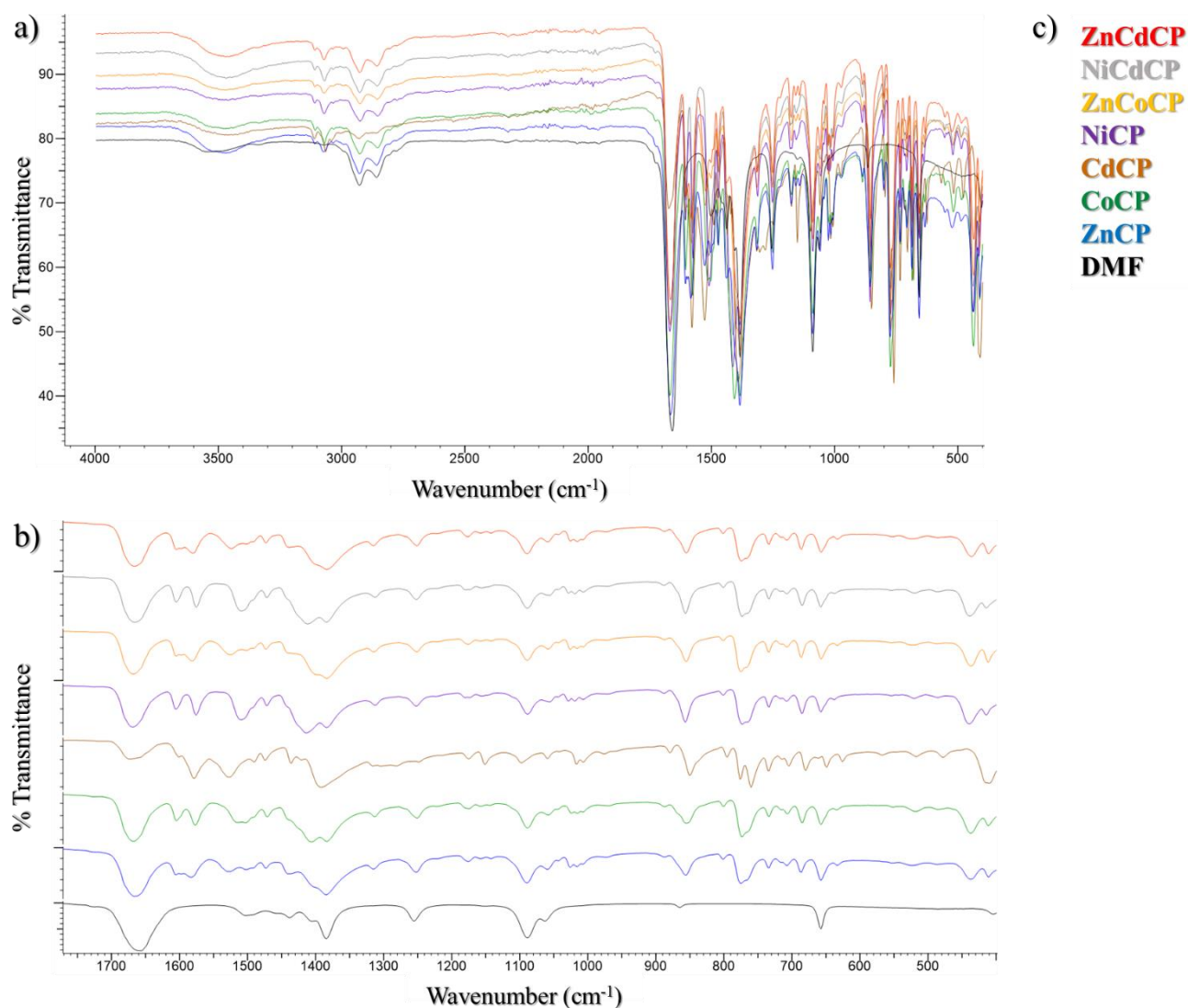
Figure S48: FT-IR spectra of all the compounds studied compared to pure DMF. In **(a)** the entire IR range is shown with spectra overlayed (slight offset from baseline). Note that the sp^3 C–H stretching bands (*ca* 3000–2800 cm^{-1}) are purely derived from the guest, while the aromatic sp^2 C–H stretching bands (*ca* 3200–3000 cm^{-1}) are in turn derived from the host system. The fingerprint region of the spectra are shown stacked in **(b)**. The legend for both **(a)** and **(b)** is represented in **(c)**.

7. Thermogravimetric analysis (TGA)

TGA data were recorded by measuring the percentage mass as the sample was heated at a constant rate. A TA Instruments Q500 thermogravimetric analyser was used. Samples were placed in aluminium pans and sample weights typically ranged from 1 to 5 mg. N_2 gas (flow rate 40 ml min^{-1}) was used to purge the furnace. The temperature was ramped from room temperature to *ca.* 600 °C at a constant heating rate of 10 °C min^{-1}. The resulting thermograms were analysed using the TA Instruments Universal Analysis program.
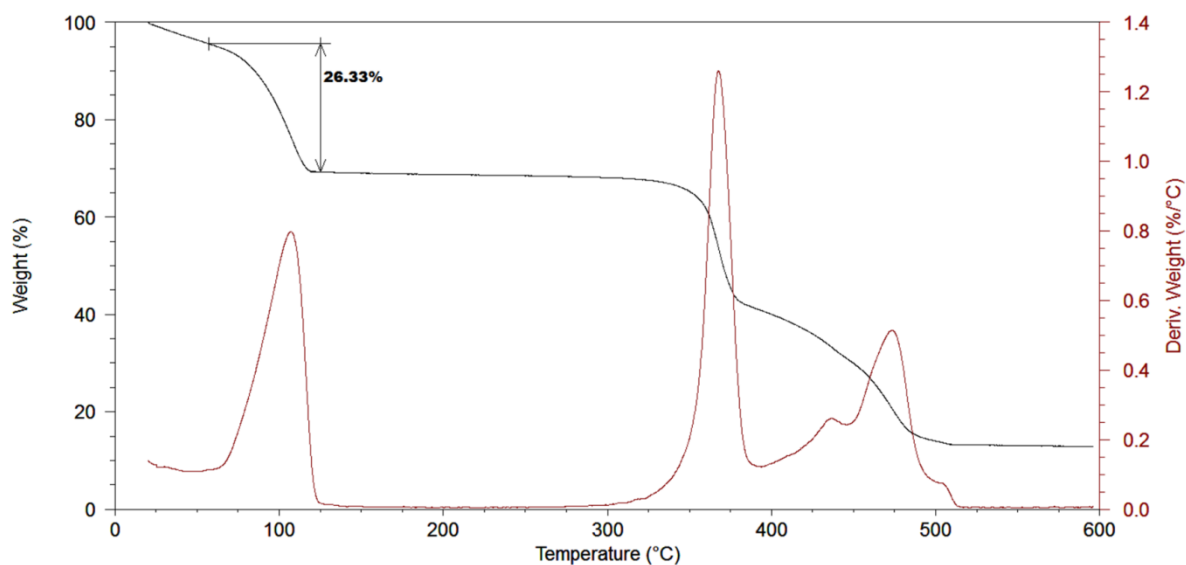
Figure S49: Thermogram of **ZnCP^{HT}**. The weight loss of 26.3% corresponds to *ca* two DMF molecules per host formula unit (calculated 24.0%).
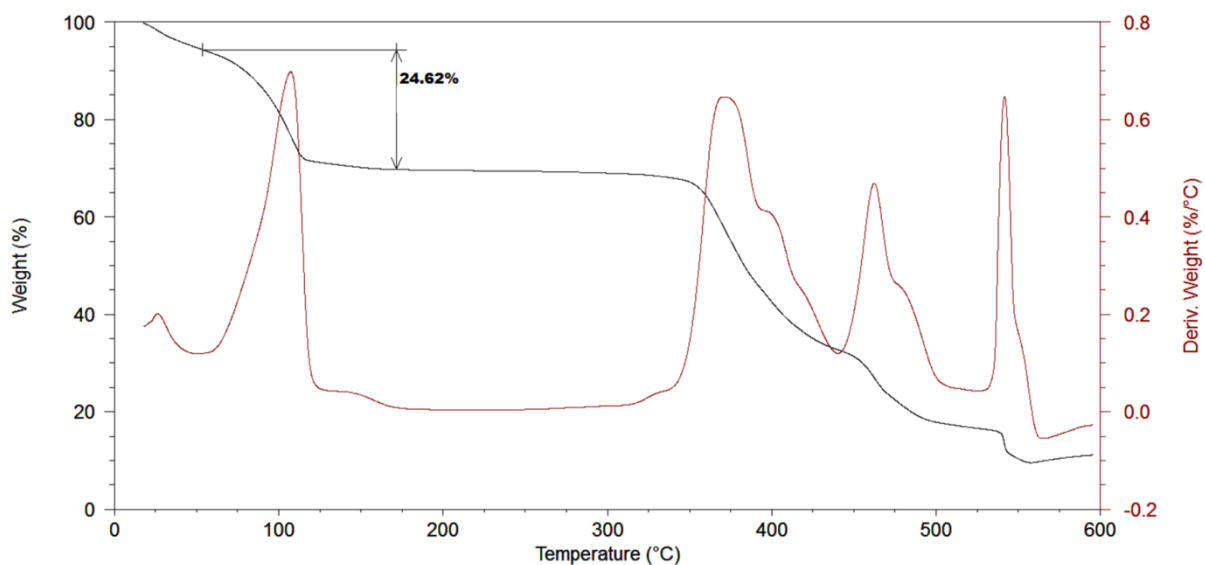
Figure S50: Thermogram of **CoCP^{HT}**. The weight loss of 24.6% corresponds to *ca* two DMF molecules per host formula unit (calculated 24.3%).
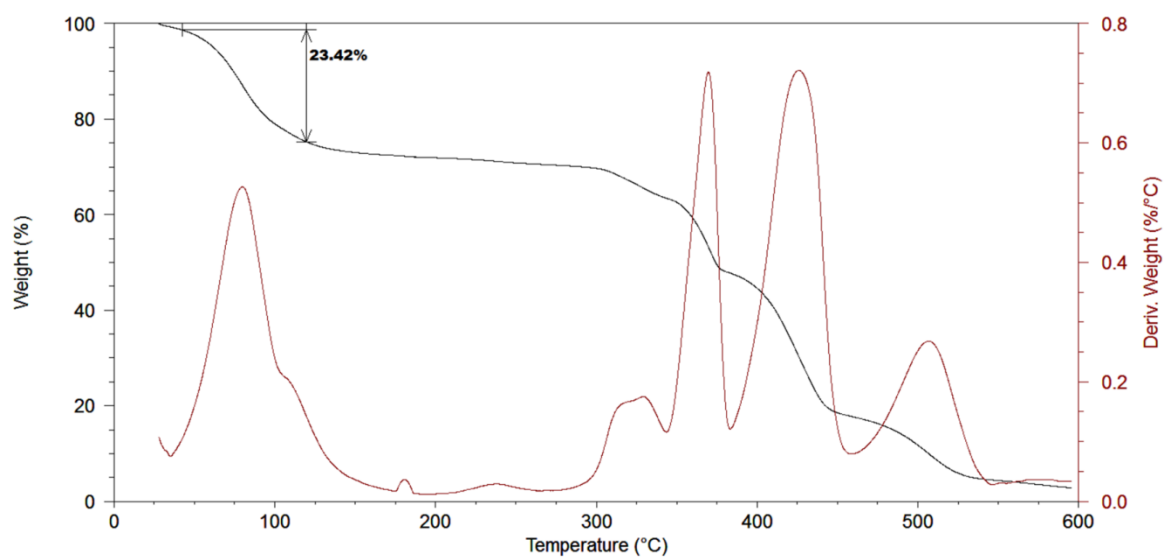
Figure S51: Thermogram of **CdCP**^{HT}. The weight loss of 23.4% corresponds to *ca* two DMF molecules per host formula unit (calculated 22.3%).
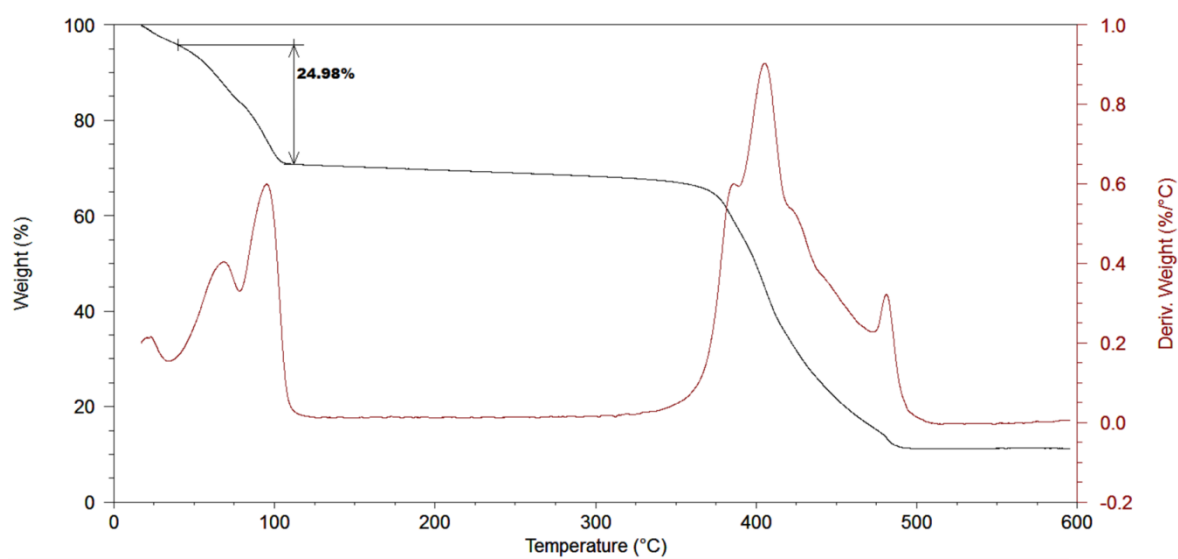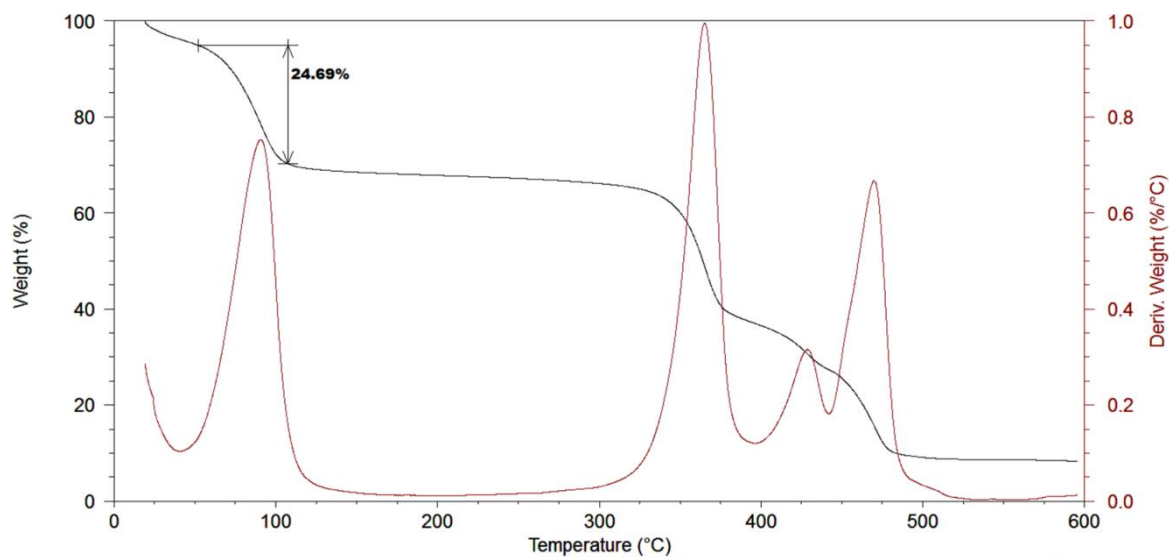

Figure S52: Thermogram of **NiCP**^{HT}. The weight loss of 25.0% corresponds to *ca* two DMF molecules per host formula unit (calculated 24.3%).

Figure S53: Thermogram of **ZnCoCP^{HT}**. The weight loss of 24.7% corresponds to *ca* two DMF molecules per host formula unit (calculated 24.1%).
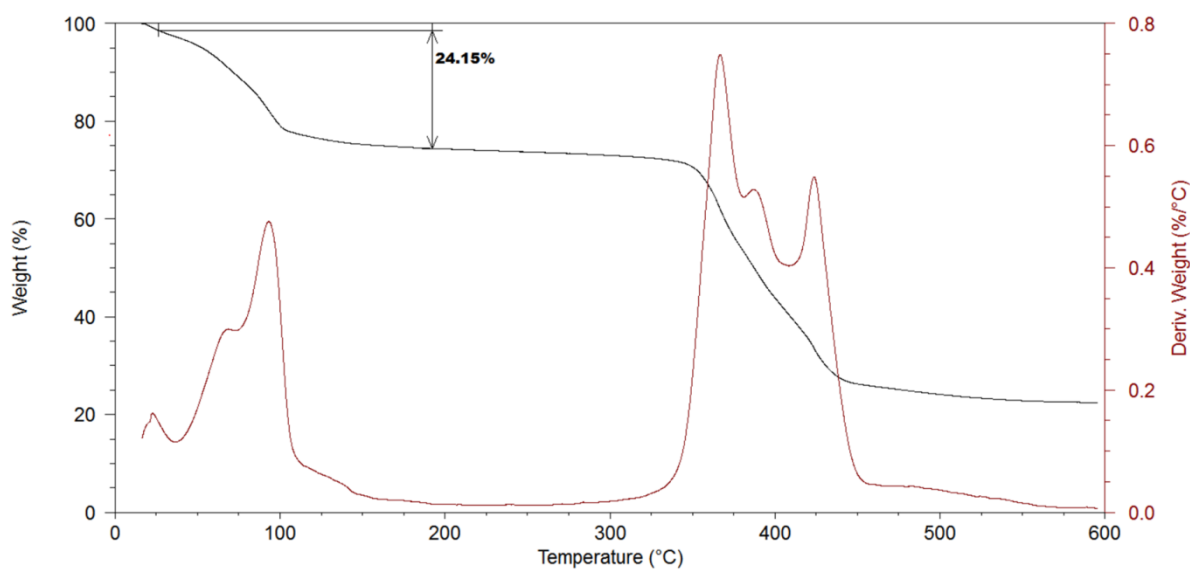

Figure S54: Thermogram of **NiCdCP^{HT}**. The weight loss of 24.2% corresponds to *ca* two DMF molecules per host formula unit (calculated 23.8%).
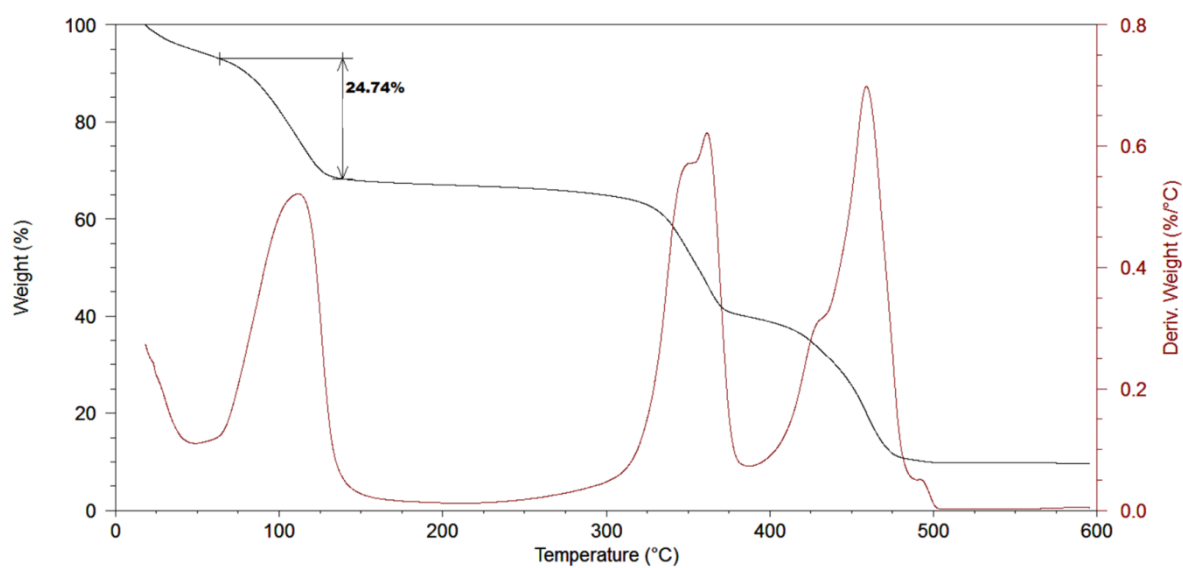
Figure S55: Thermogram of **ZnCdCP**^{HT}. The weight loss of 24.7% corresponds to *ca* two DMF molecules per host formula unit (calculated 23.9%).

8. Energy dispersive X-ray spectroscopy (EDX)

Samples of **ZnCoCP**, **ZnCdCP** and **NiCdCP** were prepared for EDX analysis by removing the guest in a thermogravimetric furnace (T_{max} = 150 °C, ramp rate = 5 °C min^{-1}, N$_2$ purge = 40 ml min^{-1}). This produced single crystals of the guest-free phases of these materials – denoted **ZnCoCPa**, **ZnCdCPa** and **NiCdCPa**. Samples were attached to aluminium scanning electron microscope (SEM) stubs using double sided carbon tape. The samples were allowed to dry in an oven, after which a gold sputter coating (10 nm) was applied. Images were recorded out with a Zeiss EVO SEM equipped with both a backscattered electron detector (Carl Zeiss Microscopy, Germany) and an energy dispersive X-ray spectroscopy (EDX) detector (Oxford Instruments® XMax 20 mm^2). Accelerating voltage (EHT): 20 kV, working distance: 8.5 mm and beam current: 11 nA. Measurements were carried out in triplicate.

Table S18. Molar ratios for solid solutions determined by EDX.

Material	Ratio in crystallisation solution (Zn:Co:Cd:Ni)	Zinc	Cobalt	Cadmium	Nickel
ZnCoCPa	1:1:0:0	0.145(5)	0.012(1)	0	0
ZnCdCPa	1:0:1:0	0.149(12)	0	0.012(1)	0
NiCdCPa	0:0:1:1	0	0	0.029(1)	0.156(9)

The final ratios were determined to be approximately 12:1 Zn:Co, 12:1 Zn:Cd and 5:1 Ni:Cd for **ZnCoCP**, **ZnCdCP** and **NiCdCP**, respectively.

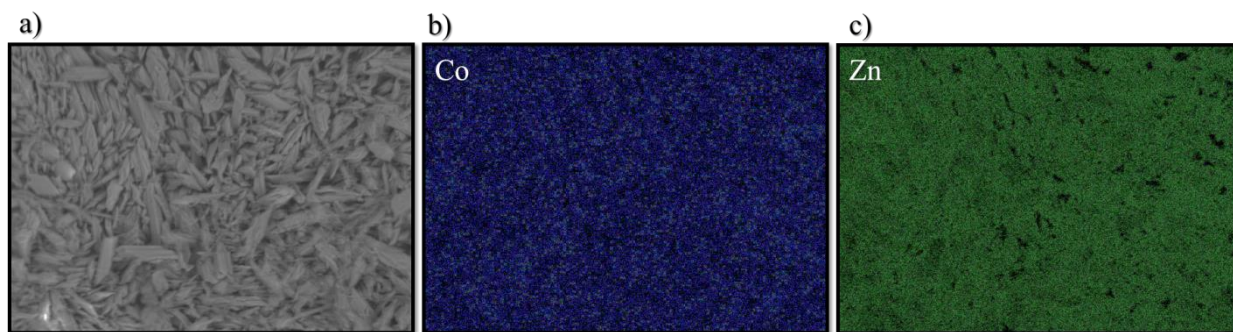## 8.1. EDX mapping

Figure S56: SEM imaging of **ZnCoCPa (a)** along with EDX mapping showing the distribution of the cobalt **(b)** and zinc **(c)** atoms in the sample. The metal atoms are evenly distributed throughout the sample, with a higher concentration of zinc.

Figure S57: SEM imaging of **ZnCdCPa (a)** along with EDX mapping showing the distribution of the cadmium **(b)** and zinc **(c)** atoms in the sample. The metal atoms are evenly distributed throughout the sample, with a higher concentration of zinc.
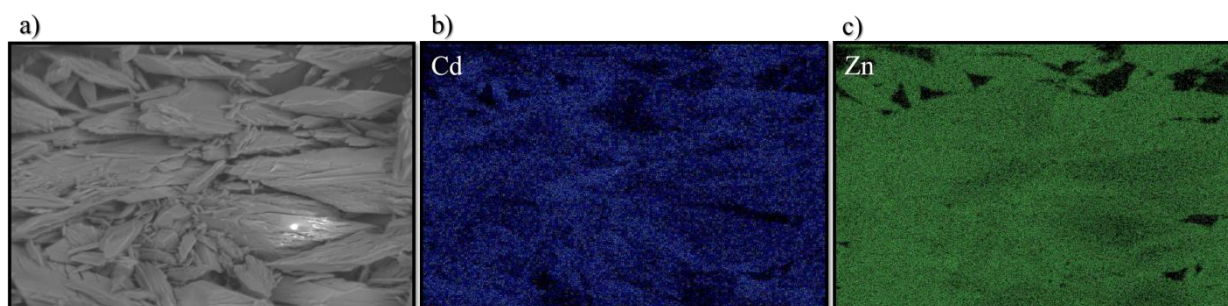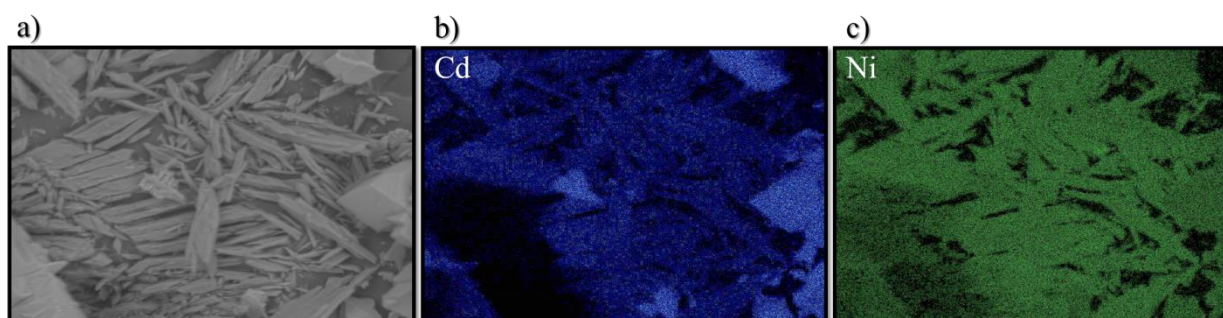

Figure S58: SEM imaging of **NiCdCPa (a)** along with EDX mapping showing the distribution of the cadmium **(b)** and nickel **(c)** atoms in the sample. The metal atoms are evenly distributed throughout the sample, with a higher concentration of nickel.

References

1   MiTeGen, MiTeGen, https://www.mitegen.com/, (accessed 25 June 2018).

2   Bruker AXS Inc., 2016.

3   Bruker AXS Inc., 2016.

4   G. M. Sheldrick, *Acta Cryst.*, 2015, **A71**, 3–8.

5   G. M. Sheldrick, *Univ. Göttingen, Germany*, 2018.

6   L. J. Barbour, *J. Supramol. Chem.*, 2001, **1**, 189–191.

7   L. J. Barbour, *J. Appl. Cryst.*, 2020, **53**, 1–6.

8   Persistence of Vision Raytracer Pty. Ltd., 2004.

9   C. F. Macrae, P. R. Edgington, P. McCabe, E. Pidcock, G. P. Shields, R. Taylor, M. Towler and J. Van De Streek, *J. Appl. Crystallogr.*, 2006, **39**, 453–457.

10   C. F. Macrae, I. J. Bruno, J. A. Chisholm, P. R. Edgington, P. McCabe, E. Pidcock, L. Rodriguez-Monge, R. Taylor, J. Van De Streek and P. A. Wood, *J. Appl. Crystallogr.*, 2008, **41**, 466–470.

11   C. F. MacRae, I. Sovago, S. J. Cottrell, P. T. A. Galek, P. McCabe, E. Pidcock, M. Platings, G. P. Shields, J. S. Stevens, M. Towler and P. A. Wood, *J. Appl. Crystallogr.*, 2020, **53**, 226–235.

12   A. L. Spek, *Acta Crystallogr.*, 2015, **C71**, 9–18.

13   D. P. van Heerden and L. J. Barbour, *Chem. Soc. Rev.*, 2021, **50**, 735–749.

14   Bruker AXS Inc., *Bruker AXS Inc., Wisconsin, USA*, 2016.

15   M. J. Cliffe and A. L. Goodwin, *J. Appl. Crystallogr.*, 2012, **45**, 1321–1329.

16   B. Dwivedi, A. Shrivastava, L. Negi and D. Das, *Cryst. Growth Des.*, 2019, **19**, 2519–2524.

17   D. Das, T. Jacobs and L. J. Barbour, *Nat. Mater.*, 2010, **9**, 36–39.

18   E. R. Engel, V. J. Smith, C. X. Bezuidenhout and L. J. Barbour, *Chem. Commun.*, 2014, **50**, 4238–4241.

19   E. R. Engel, V. J. Smith, C. X. Bezuidenhout and L. J. Barbour, *Chem. Mater.*, 2016, **28**, 5073–5079.

20   A. D. Fortes, E. Suard and K. S. Knight, *Science*, 2011, **331**, 742–746.

21   M. K. Panda, T. Runčevski, A. Husain, R. E. Dinnebier and P. Naumov, *J. Am. Chem. Soc.*, 2015, **137**, 1895–1902.

22   H. Liu, M. J. Gutmann, H. T. Stokes, B. J. Campbell, I. R. Evans and J. S. O. Evans, *Chem. Mater.*, 2019, **31**, 4514–4523.

23   S. Henke, A. Schneemann and R. A. Fischer, *Adv. Funct. Mater.*, 2013, **23**, 5990–5996.

24   B. R. Mullaney, L. Goux-Capes, D. J. Price, G. Chastanet, J. F. Létard and C. J. Kepert, *Nat. Commun.*, 2017, **8**, 1–6.

25   S. J. Hunt, M. J. Cliffe, J. A. Hill, A. B. Cairns, N. P. Funnell and A. L. Goodwin, *CrystEngComm*, 2015, **17**, 361–369.

26   J. Pang, C. Liu, Y. Huang, M. Wu, F. Jiang, D. Yuan, F. Hu, K. Su, G. Liu and M. Hong, *Angew. Chem., Int. Ed.*, 2016, **55**, 7478–7482.

27   H. L. Zhou, Y. B. Zhang, J. P. Zhang and X. M. Chen, *Nat. Commun.*, 2015, **6**, 1–7.

28   J. X. Hu, Y. Xu, Y. S. Meng, L. Zhao, S. Hayami, O. Sato and T. Liu, *Angew. Chem., Int. Ed.*, 2017, **56**, 13052–13055.

29   B. K. Saha, S. A. Rather and A. Saha, *Eur. J. Inorg. Chem.*, 2017, **28**, 3390–3394.

30   J. S. Ovens and D. B. Leznoff, *Inorg. Chem.*, 2017, **56**, 7332–7343.

31   J. E. Auckett, S. G. Duyker, E. I. Izgorodina, C. S. Hawes, D. R. Turner, S. R. Batten and V. K. Peterson, *Chem. - A Eur. J.*, 2018, **24**, 4774–4779.

32   A. L. Goodwin, M. Calleja, M. J. Conterio, M. T. Dove, J. S. O. Evans, D. A. Keen, L. Peters and M. G. Tucker, *Science*, 2008, **319**, 794–797.

33   W. Cai and A. Katrusiak, *Nat. Commun.*, 2014, **5**, 1–8.

34   Q. Ren, W. Hutchison, J. Wang, A. Studer, G. Wang, H. Zhou, J. Ma and S. J. Campbell, *ACS Appl. Mater. Interfaces*, 2019, **11**, 17531–17538.